

Model of thermal wave-front distortion in interferometric gravitational-wave detectors. I. Thermal focusing

Raymond G. Beausoleil,* Eric K. Gustafson, and Martin M. Fejer

Edward L. Ginzton Laboratory, Stanford University, Stanford, California 94305

Erika D'Ambrosio, William Kells, and Jordan Camp

Laser Interferometer Gravitational Wave Observatory Project, California Institute of Technology, Pasadena, California 91125

Received December 2, 2002

We develop a steady-state analytical and numerical model of the optical response of power-recycled Fabry–Perot Michelson laser gravitational-wave detectors to nonlinear thermal focusing in optical substrates. We assume that the thermal distortions are small enough that we can represent all intracavity fields as linear combinations of basis functions derived from the eigenmodes of a Fabry–Perot arm cavity. We have included the effects of power absorption in optical substrates and coatings, mismatches between laser wave-front and mirror surface curvatures, and aperture diffraction. We demonstrate a detailed numerical example of this model using the MATLAB program Melody for the initial Laser Interferometer Gravitational Wave Observatory detector. © 2003 Optical Society of America

OCIS codes: 000.2780, 000.4430, 140.4780, 190.4870, 350.1270, 350.6830.

1. INTRODUCTION

In the present decade, a number of long-baseline laser interferometers are expected to become operational and to begin a search for astrophysical sources of gravitational radiation.^{1–3} These include the Laser Interferometer Gravitational Wave Observatory^{4,5} (LIGO), the VIRGO project,⁶ the GEO 600 project,⁷ and the TAMA 300 project.⁸ All of these detectors will employ a variant of a Michelson interferometer illuminated with stabilized laser light. The light will be phase modulated at one or more radio frequencies, producing modulation sidebands about the carrier frequency that provide a phase reference for sensing small variations of the interferometer arm lengths.⁹ Gravitational radiation will produce a differential length change in the arms of the Michelson interferometer, resulting in a signal at the output port.

In Fig. 1, we show the configuration of the initial LIGO detector, a power-recycled Fabry–Perot Michelson interferometer (PRFPMI). The light from a stabilized laser source enters the interferometer, which is made of an asymmetric Michelson interferometer with Fabry–Perot arm cavities. The arm cavities consist of polished input and end test masses (ITM and ETM, respectively) whose coated surfaces also act as mirrors to resonantly enhance the laser light. An additional power-recycling mirror (PRM) placed between the laser and beam splitter increases the total light power available to the arms by forming a “recycling cavity” together with the beam splitter and arm-cavity input mirrors. The sideband frequency and interferometer lengths are adjusted so that the sidebands resonate in the recycling cavity but not in the arms, while the carrier resonates in both sets of cavi-

ties. This allows extraction of control signals for all four length degrees of freedom.¹⁰

The noise level in the detection band at the interferometer output port must be held below the required strain sensitivity. The primary noise sources limiting the interferometer sensitivity are seismic noise at frequencies below 100 Hz, thermal noise between roughly 100 and 300 Hz, and photon-counting noise at frequencies greater than 300 Hz. Photon-counting noise is suppressed by use of sufficient laser power; a design strain sensitivity of roughly 10^{-21} over a time period of a millisecond will require a power of several hundred watts incident on the beam splitter.

A concern in the operation of an interferometer at such high power levels is optical distortion. The presence of absorption in the coatings and substrates of the optics can give rise to nonuniform heating due to the Gaussian intensity profile of the laser light. This heating will cause a temperature rise in the substrate, which, coupled to the temperature dependence of the substrate index of refraction, will cause a distortion of the wave front of the light transmitted through the substrate. For example, the initial LIGO design provides for fused-silica input test masses that are 10 cm thick. To ensure the stability of the arm-cavity resonant mode, the ITM radius of curvature is set to be several times the length of the arm cavity, or of order 10 km. By comparison, the substrate heating due to a nominal substrate and coating absorption of 5 ppm/cm and 1 ppm (parts per million), respectively, causes the generation of a thermal lens in the substrate with a nominal focal length of 8 km. This significant distortion can have important consequences for both the

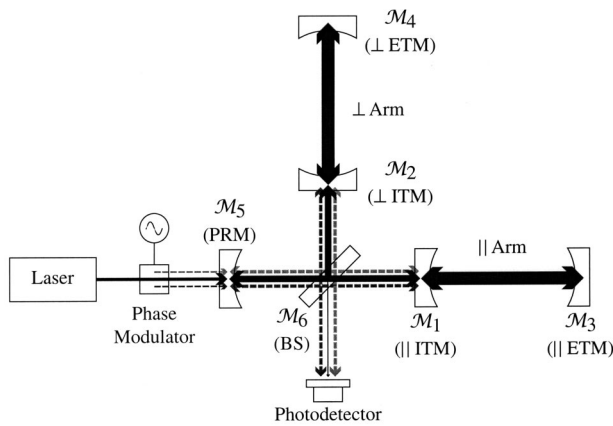


Fig. 1. Schematic configuration of the initial LIGO detector, a power-recycled Fabry-Perot Michelson interferometer (PRF-PMI).

power buildup of the RF sidebands in the recycling cavity and the interferometer sensitivity.

There have been a number of efforts made to understand the effects of the propagation of distorted wave fronts through gravitational-wave interferometers, including an approximate treatment of wave-front distortion in power-recycled and dual-recycled systems due to imperfections in the shape or alignment of some optical components,¹¹ an approximate treatment of thermal lensing and surface deformation in early Fabry-Perot Michelson designs,¹² and an approximate description of thermal lensing in alternate signal-extraction designs.^{13,14} Each of these discussions emphasized the effects of optical distortion on a particular subset of the optical performance characteristics of an interferometer. In principle, fast Fourier transform (FFT) methods^{15–17} can be used to simulate a thermally loaded interferometer, but the computational cost of an iterated self-consistent FFT numerical analysis of the corresponding intracavity fields would be prohibitive.

By contrast, we have developed a flexible and robust analytical and numerical model of the effects of wave-front distortion on the optical performance of a gravitational-wave interferometer that requires far fewer computational resources than an FFT approach. The model includes accurate contributions to the thermal distortions in all substrates due to optical absorption in the substrate and both coatings of each test mass,¹⁸ the effects of any mismatch between the curvatures of the laser wave front and the mirror surface at each reflection, and the diffraction by an aperture at each instance of reflection and transmission. Operators representing these physical effects on the reflection and transmission properties of mirrors and beam splitters are explicitly incorporated into a set of transfer (or scattering) matrices that relate output fields to input fields incident on the surfaces of those elements. The corresponding transfer matrices of more complex optical components (e.g., a Fabry-Perot interferometer) can subsequently be constructed in a hierarchical fashion from those of simpler systems. With this approach, the model determines a self-consistent steady-state solution to the interferometer power buildup in the presence of optical distortion and employs an inter-

nal numerical mechanism to preserve the nearly ideal longitudinal phase-resonance conditions that would otherwise be provided by an external servo-locking control system. We have developed computer code representing this model that is sufficiently flexible to allow new physical effects to be added to the simulations with a modicum of effort and that can be stopped, interrogated, and restarted at any stage of a simulation. Our implementation of the artificial resonance-locking mechanism provides an exponential reduction in the execution time required for a self-consistent simulation by dynamically adjusting the frequency response of the interferometer.

Our current model employs basis-function expansions of the electromagnetic field everywhere in the interferometer.^{19–22} In principle, these basis functions can be spatial eigenfunctions of the interferometer, but in practice, imperfect mode matching of the multiple cavities comprising the full interferometer and the presence of apertures in the system means that round-trip spatial propagators are *not* Hermitian, and the eigenfunctions are not power orthogonal.^{23–25} Therefore we choose an expansion of the intracavity field in an arbitrary set of power-orthogonal unperturbed spatial basis functions that are not necessarily eigenfunctions of any subsystem of a thermally loaded, perturbed interferometer. Since we can move from one spatial representation to another simply by recomputing the propagator matrix elements, the relative merit of a set of possible basis choices is determined by the number of basis modes needed to describe the intracavity field accurately. Our analysis of the operators encapsulating the physics of the perturbative phenomena described in the model is invariant under such a change of spatial basis. Nevertheless, the choice of an incomplete subset of basis functions inevitably introduces false optical losses because power is transferred to higher-order spatial modes that are not included in a necessarily finite numerical simulation. Therefore we introduce unitary approximations for nondiffractive operators that monotonically improve as more basis functions are included in the simulation.

In Section 2 of this paper, we describe our representation of the intracavity electromagnetic field and the operators incorporated into the transfer matrices of the subsystems comprising components of typical interferometric gravitational-wave detectors. We develop a unitary approximation for nondiffractive operators expanded in finite-dimensional basis sets, and, in our discussions of the Fabry-Perot and Michelson interferometers, we introduce abstract idealizations of the control systems needed to maintain different intracavity resonance conditions. In Section 3, using these building blocks, we construct a model of the initial LIGO interferometer, and we point out that the basis functions chosen for a matrix description of the interferometer need not be spatial eigenfunctions of the fully coupled resonators. As a preliminary verification of our method, we compare the predictions of our numerical implementation of this model in a set of well-defined linear test cases with the output generated by a fast-Fourier-transform computer-code suite. Finally, we simulate the optical performance of the initial LIGO interferometer under full thermal load, using a straightforward nonlinear solution method

that computes the steady-state fields everywhere in the system after only a few seconds on an ordinary desktop computer.

2. MODELS OF OPTICAL COMPONENTS AND STRUCTURES

A. Representation of the Electromagnetic Field

Throughout this work, we represent a propagating laser electric field $\mathbf{E}(\mathbf{r}, t)$ with angular carrier frequency ω_0 as the real part of a product of a real time-independent polarization unit vector \mathbf{e} , a complex amplitude function $E(\mathbf{r}, t)$, and the carrier wave function $\exp[i(k_0 z - \omega_0 t)]$, where $\lambda_0 = 2\pi/k_0 = 2\pi c/\omega_0$ is the laser wavelength²²:

$$\mathbf{E}(\mathbf{r}, t) = \text{Re}\{\mathbf{e}E(\mathbf{r}, t)\exp[i(k_0 z - \omega_0 t)]\}. \quad (1)$$

We use the amplitude function $E(\mathbf{r}, t)$ to represent any closely spaced frequency components (such as radio-frequency-modulated sidebands) as

$$E(\mathbf{r}, t) = \sum_q E_q(\mathbf{r}, t)\exp[i(k_q z - \omega_q t)], \quad (2)$$

where the summation is taken over all frequency components (including the carrier), $E_q(\mathbf{r}, t)$ is the complex-amplitude function of component q , $\omega_q = k_q/c \equiv \omega_0 + \Delta\omega_q$ is the angular frequency of component q , and $\Delta\omega_q \equiv \Delta k_q/c \ll \omega_0$ is the angular frequency shift of component q . By convention, the carrier is labeled by $q = 0$, and therefore $\Delta\omega_0 = 0$. We express all field amplitudes in units of $(\text{W}/\text{cm}^2)^{1/2}$, so that the time-averaged intensity carried by $\mathbf{E}(\mathbf{r}, t)$ is $\bar{I}(\mathbf{r}, t) = \frac{1}{2}\sum_q |E_q(\mathbf{r}, t)|^2$.

We will represent the transverse spatial dependence of the field amplitude $E_q(\mathbf{r}, t)$ at any propagation plane within a laser interferometric gravitational-wave detector as a linear superposition of a set of amplitude basis functions with fixed transverse spatial profiles. In general, these amplitudes are eigenfunctions of a non-Hermitian integral transform equation (generally a composition of many consecutive integral transforms, each of which carries the field from one aperture to the next) that describes round-trip propagation through a specific resonant subsystem of the unperturbed interferometer. These resonant eigenfunctions can then be propagated throughout the remainder of the interferometer, defining a unique set of spatial basis functions.²² Therefore given the existence of a numerically complete set of these transverse spatial eigenfunctions, we can expand the sideband amplitude function as

$$E_q(\mathbf{r}, t) = \sum_{mn} E_{mnq}(z, t)u_{mn}(\mathbf{r}). \quad (3)$$

Hence we can convert any composition of two consecutive integral transforms into a simple matrix product. In practice, we are interested in the steady-state characteristics of the detector under thermal load, and we will clearly indicate the propagation plane under discussion, so we will usually suppress the explicit coordinates $\{z, t\}$ in later sections.

As an example, consider the simple case of laser field propagation through a distance $L \equiv z_2 - z_1$ in vacuum. Suppose that we choose to represent the spatial and tem-

poral properties of this field using N transverse eigenfunctions $u_{mn}(\mathbf{r})$ and Q frequency components, including the carrier and both positive and negative sidebands for each nonzero radio modulation frequency. We arrange the expansion coefficients into an $N \times Q$ ordered matrix E with elements E_{mnq} , where each row represents the spatial eigenfunction corresponding to a particular choice of $\{m, n\}$ and each column corresponds to a particular frequency component q , and we assume that L has been chosen to provide resonant excitation of the fundamental carrier spatial mode E_{000} . In this basis, the spatial contribution to the vacuum propagation kernel is given by an $N \times N$ diagonal matrix G with elements

$$G_{mn,m'n'} = \exp(i\Delta\varphi_{mn})\delta_{mm'}\delta_{nn'}, \quad (4)$$

where $\Delta\varphi_{mn} \equiv \varphi_{mn} - \varphi_{00}$ is the net Gouy phase (relative to the fundamental spatial mode) accumulated by mode mn over the propagation distance L , and the net longitudinal optical path-length contribution (relative to the carrier) is given by a $Q \times Q$ diagonal matrix Ω with elements

$$\Omega_{qq'} = \exp(i\Delta\omega_q \tau)\delta_{qq'}, \quad (5)$$

where $\tau \equiv L/c$ is the propagation time. The components of the field following the propagation step can then be computed with the sparse matrix product

$$E(z_2) = GE(z_1)\Omega. \quad (6)$$

We are particularly interested in the more complex example of a power-recycled Fabry–Perot Michelson laser gravitational-wave interferometer. In its unperturbed state (i.e., in the absence of aperture diffraction and thermal wave-front distortions), this detector configuration is described well by Hermite–Gauss basis functions under perfect mode-matching conditions. The infinite-aperture Hermite–Gauss basis is orthonormal (since it is generated by a Hermitian propagation equation); thus field amplitude expansions that use this basis are power orthogonal,²³ allowing time-averaged intensities to be calculated with the sum of the inner products $|E_q(\mathbf{r}, t)|^2 = \sum_{mn} |E_{mnq}(z, t)|^2$. If both Gouy and optical path-length phase contributions are accumulated with Eq. (6), then we can represent an arbitrary nonastigmatic Hermite–Gauss basis function $u_{mn}(x, y)$ at a given reference plane using

$$u_{mn}(x, y) = \left(\frac{1}{2^{m+n}m!n!} \frac{2}{\pi w^2}\right)^{1/2} H_m\left(\frac{\sqrt{2}x}{w}\right) H_n\left(\frac{\sqrt{2}y}{w}\right) \times \exp\left[i\left(\frac{k}{2R} - \frac{1}{w^2}\right)(x^2 + y^2)\right], \quad (7)$$

where $H_n(x)$ is the Hermite polynomial of order n , w is the beam spot radius, and R is the wave-front radius of curvature at that reference plane. Throughout this work, we will define the x – z plane to be “horizontal,” containing the central beam paths of the two Fabry–Perot arm cavities in Fig. 1, and the y – z plane to be “vertical,” perpendicular to the horizontal plane and parallel to the local gravity gradient of the Earth.

B. Mirrors

1. Aperture-Diffraction and Mirror-Field Curvature Mismatch Operators

Consider the general problem of the reflection of a propagating electromagnetic field by a perfectly reflecting cylindrically symmetric mirror \mathcal{M} with spherical radius of curvature R_M and aperture diameter $2a$. The reflection can be described in a single step taken from the aperture \mathcal{A} at the reference plane $z^<$ conventionally located just *before* the reflection from \mathcal{M} to the field position $z^>$ just *after* reflection has occurred. If the transverse field at $z^<$ is $E(x', y', z^<)$, then the corresponding field at $z^>$ is given by Huygens's integral in the Fresnel approximation as²⁴

$$E(x, y, z^>) = \int_{\mathcal{A}} dx' dy' K(x, y; x', y') E(x', y', z^<), \quad (8)$$

where the functional form of the forward-propagation kernel for a cylindrically symmetric mirror is²²

$$K(x, y; x', y') = -\exp\left[-i \frac{\pi}{\lambda_0} \frac{2}{R_M} (x'^2 + y'^2)\right] \times \delta(x - x') \delta(y - y'), \quad (9)$$

where λ_0 is the vacuum carrier wavelength. Note that we have (temporarily) neglected an overall negative sign that accounts for the Maxwell boundary condition at the perfectly reflecting mirror surface.

If we expand the field at both reference planes using a numerically complete set of Cartesian basis functions as in Eq. (3), then we can compute the matrix elements of the forward-propagation kernel in that basis as

$$\begin{aligned} K_{mn, m'n'} &= \int \int_{-\infty}^{\infty} dx dy \int \int_{\mathcal{A}} dx' dy' K(x, y; x', y') \\ &\quad \times u_{mn}^\dagger(x, y, z^>) u_{m'n'}(x', y', z^<) \\ &= \int \int_{\mathcal{A}} dx dy \exp\left[-i \frac{\pi}{\lambda_0} \frac{2}{R_M} (x^2 + y^2)\right] \\ &\quad \times u_{mn}^\dagger(x, y, z^>) u_{m'n'}(x, y, z^<). \end{aligned} \quad (10)$$

Here the function $u_{mn}^\dagger(x, y, z^>)$ is *not* generally the conjugate transpose of $u_{mn}(x, y, z^>)$. Instead, these basis functions represent fields propagating through the system in the *reverse* direction and are obtained by

solving the Huygens–Fresnel integral Eq. (8) with $K^T(x, y; x', y')$, the transpose of the forward-propagation kernel.^{22–24}

Although the reflection-diffraction problem is specified completely by Eq. (10), it can introduce inconsistencies in practical implementations of optical resonator simulations. For example, when a finite number of basis functions are used to represent the propagating field, the matrix calculated with Eq. (10) generates two sources of optical loss: genuine diffraction loss due to field truncation by the aperture, and power transferred to higher-order optical modes that are ignored in the simulation. The latter contribution is unphysical: in the limit $a \rightarrow \infty$, when a numerically complete set of basis functions is used, the propagation matrix must conserve energy (i.e., must be unitary). Therefore for the purposes of our simulations, we will explicitly allow diffraction loss due to aperture truncation only, and we separate the effects of aperture diffraction and reflection into two consecutive propagation steps using the formulation

$$K \equiv CA, \quad (11)$$

where A is a matrix operator representing purely transmissive aperture diffraction, and C is a unitary matrix operator describing direct focusing by a spherical mirror at normal incidence.

As a concrete example, we first calculate the matrix elements of A in the Hermite–Gauss basis, treating the truncation as a perturbation and describing the field both before and after the aperture using a linear superposition of a finite set of unperturbed Hermite–Gauss functions. Therefore $u_{mn}^\dagger(x, y) = u_{mn}^*(x, y)$, and we define the analytical integral

$$\begin{aligned} A_{mn, m'n'} &= \int \int_{\mathcal{A}} dx dy u_{mn}^*(x, y) u_{m'n'}(x, y) \\ &= \delta_{m, m'} \delta_{n, n'} - \exp(-\alpha) I_{mn, m'n'}(\alpha), \end{aligned} \quad (12)$$

where $\alpha = 2(a/w)^2$, and the integration is performed over the circular aperture defined by $(x^2 + y^2)^{1/2} \leq a$. We specify a basis set by designating the transverse modes for a given frequency component q in order of increasing $m + n$ first, and then in order of increasing n . For example, if we use a Hermite–Gauss basis with $m + n \leq 2$, then for the column vector $E_q \equiv \{E_{00q}, E_{10q}, E_{01q}, E_{20q}, E_{11q}, E_{02q}\}^T$, we obtain the matrix

$$I(\alpha) = \begin{bmatrix} 1 & 0 & 0 & \frac{1}{\sqrt{2}}\alpha & 0 & \frac{1}{\sqrt{2}}\alpha \\ 0 & 1 + \alpha & 0 & 0 & 0 & 0 \\ 0 & 0 & 1 + \alpha & 0 & 0 & 0 \\ \frac{1}{\sqrt{2}}\alpha & 0 & 0 & 1 + \frac{1}{2}\alpha + \frac{3}{4}\alpha^2 & 0 & \frac{1}{4}\alpha(\alpha - 2) \\ 0 & 0 & 0 & 0 & 1 + \alpha + \frac{1}{2}\alpha^2 & 0 \\ \frac{1}{\sqrt{2}}\alpha & 0 & 0 & \frac{1}{4}\alpha(\alpha - 2) & 0 & 1 + \frac{1}{2}\alpha + \frac{3}{4}\alpha^2 \end{bmatrix}. \quad (13)$$

Note that nonzero elements of $I(\alpha)$ satisfy the relation $I_{mn,m'n'}(\alpha) \approx O[\alpha^{\frac{1}{2}(m+n+m'+n')}]$.

Next, we ignore aperture diffraction and calculate the matrix elements of C in the Hermite–Gauss basis. Strictly speaking, the matrix elements of C can be calculated with Eq. (10) in the limit $a \rightarrow \infty$. However, as described above, we seek an explicitly unitary approximation for C that monotonically improves as we include more basis functions in the field expansion. When Eq. (10) is applied to a Hermite–Gauss basis function with field curvature parameter R_F , this parameter is transformed according to the $ABCD$ propagation law as $1/R_F' = 1/R_F - 2/R_M$. In the unperturbed case where $R_M = R_F$, the curvature parameter of the backward-propagating basis function is therefore $-(-R_F) = R_F$, and, using Eq. (7), we have

$$C \equiv \exp(i\gamma c), \quad (14)$$

where

$$\begin{aligned} \gamma &\equiv \frac{\pi w^2}{\lambda_0} \left(\frac{1}{R_F} - \frac{1}{R_M} \right), \\ c_{mn,m',n'} &\equiv \frac{2}{w^2} \int \int_{-\infty}^{\infty} dx dy (x^2 + y^2) \\ &\quad \times |u_{mn}(x, y) u_{m'n'}(x, y)|. \end{aligned} \quad (15)$$

As the number of Hermite–Gauss basis functions used to represent E_q grows, $\exp(i\gamma c) \rightarrow C$, and since c is symmetric, $\exp(i\gamma c)$ is explicitly unitary. Using the generating function of the Hermite polynomials, we obtain the matrix elements

$$c_{mn,m'n'} = X_{m,m'}^2 \delta_{n,n'} + \delta_{m,m'} X_{n,n'}^2, \quad (17)$$

where

$$\begin{aligned} X_{m,m'}^2 &\equiv \frac{1}{2} (1 + 2m) \delta_{m,m'} \\ &\quad + \frac{1}{2} \sqrt{(m' + 1)(m' + 2)} \delta_{m,m'+2} \\ &\quad + \frac{1}{2} \sqrt{(m + 1)(m + 2)} \delta_{m',m+2}. \end{aligned} \quad (18)$$

As a straightforward test of our unitary approximation, we can compare the separated propagator given by Eq. (11) with the exact propagator specified by Eq. (10) for the TEM_{00} Hermite–Gauss mode. An explicit calculation with Eq. (10) yields

$$K_{00,00} = \frac{1 - \exp[-(1 + i\gamma)\alpha]}{1 + i\gamma}. \quad (19)$$

In Fig. 2, we plot the fractional error in $|K_{00,00}|$ accrued by computing $K = C A$, where A is provided by Eq. (12) and C by Eq. (14). For an incident field with a spot radius $w = 3.64$ cm and a wave-front radius of curvature $R_F = 10$ km at a wavelength $\lambda = 1.0642$ μm , we show relative errors for different values of the mirror's cylindrical substrate radius and radius of curvature as a function of the maximum mode index N . The number of basis modes

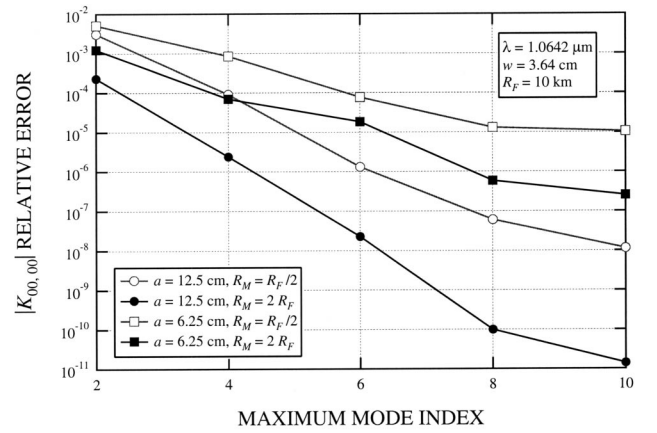


Fig. 2. Fractional error in $|K_{00,00}|$ obtained by comparing the exact value given by Eq. (19) with the TEM_{00} element of the approximate propagator $K = C A$, where A is provided by Eq. (12) and C by Eq. (14).

with $m + n \leq N$ used in the calculations of A and C is given by $\frac{1}{2}(N + 1)(N + 2)$. As we expect, the relative error decreases significantly as the number of basis modes increases.

2. Thermal-Focusing Operators

In an interferometric gravitational-wave detector, the test masses (as well as any optics that form power and/or signal recycling cavities) are thick cylindrical blocks of a transparent material, such as pure fused silica. A high-reflectance (HR) coating is applied to the broad inner face of the cylinder, forming a mirror; if transmission through the mirror substrate is necessary, then an antireflecting (AR) coating will be applied to the outer surface as well. Under test, then, laser power may be absorbed in the coatings and/or the mirror substrate (SS), and the corresponding heat flow into the substrate will result in an inhomogeneous temperature distribution throughout the mirror. This temperature gradient will cause a refractive-index gradient to form, converting the substrate into a thermally generated thick lens.

In general, the propagation of the laser field through the substrate will be described by an integral transform equation that incorporates the effects of position-dependent optical phase shifts caused by the thermal load. As discussed above, by choosing a suitable set of unperturbed basis functions (i.e., in the absence of thermal and mechanical perturbations), we can convert the integral transform equation into a scattering matrix operator that redistributes energy contained in an initial configuration of basis functions into the final set of corresponding functions that emerges from the substrate. In order to determine the elements of this matrix operator, we must first find the temperature distribution in the substrate due to absorption in both the coatings and the substrate, and then we must compute the matrix elements of the longitudinal optical path-difference (OPD) phase shift introduced by the temperature gradient.

Hello and Vinet¹⁸ have calculated both the steady-state and transient temperature distribution throughout the simplified mirror shown in Fig. 3 for the case where the change in the temperature due to the absorption of optical

power remains small compared with the external ambient temperature T_0 . This assumption linearizes the radiative boundary conditions at the surfaces of the mirror and allows the temperature increase due to coating and substrate absorption to be calculated independently (and then summed) for some incident power P . As shown in Fig. 3, they treated the mirror substrate as a thick disk spanning the cylindrical coordinates $0 \leq r \leq a$ and $-h/2 \leq z \leq h/2$, and the coating is concentrated in an infinitesimally thin layer at $z = -h/2$. After an algebraic simplification of Hello and Vinet's steady-state results, we find that the temperature distributions throughout the substrate due to absorption in the substrate and coating are, respectively,

$$T_s(r, z) = P \frac{\alpha_s a^2}{k_T} \sum_k \frac{p_k}{\zeta_k^2} \times \left[1 - 2\tau A_k \cosh\left(\zeta_k \frac{z}{a}\right) \right] J_0\left(\zeta_k \frac{r}{a}\right), \quad (20)$$

$$T_c(r, z) = P \frac{a_c a}{k_T} \sum_k p_k \times \left[A_k \cosh\left(\zeta_k \frac{z}{a}\right) - B_k \sinh\left(\zeta_k \frac{z}{a}\right) \right] J_0\left(\zeta_k \frac{r}{a}\right), \quad (21)$$

where a_c is the power absorption of the coating, α_s is the absorption coefficient of the substrate material,

$$A_k = \frac{1}{2[\zeta_k \sinh(\gamma_k) + \tau \cosh(\gamma_k)]}, \quad (22a)$$

$$B_k = \frac{1}{2[\zeta_k \cosh(\gamma_k) + \tau \sinh(\gamma_k)]}, \quad (22b)$$

$\gamma_k = \zeta_k h/2a$, $\tau = 4\epsilon\sigma T_0^3 a/k_T$, σ is the Stefan-Boltzmann constant, ϵ is the total spherical emissivity of the substrate, and k_T is the thermal conductivity of the substrate. For $a = 12.5$ cm (consistent with the value chosen for the LIGO test masses) and $T_0 = 300$ K, we

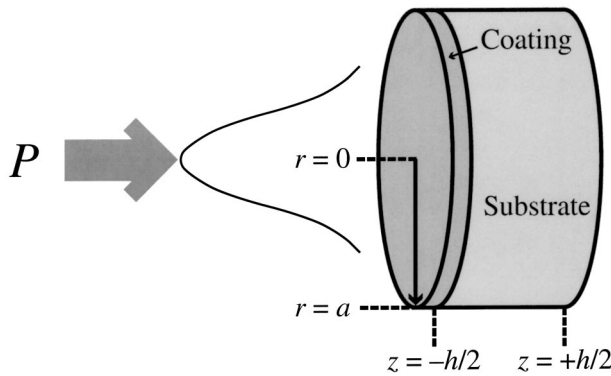


Fig. 3. Schematic diagram of a singly coated mirror and the corresponding coordinate system used by Hello and Vinet.¹⁸ Both the mirror and the incident power distribution are assumed to be azimuthally symmetric. The total incident power P can be absorbed in the coating and/or the substrate, resulting in a total temperature distribution $T(r, z)$ and a corresponding thermal lens in the substrate.

Table 1. Material Constants for Fused Silica Used in Our Simulations at $\lambda_0 = 1.0642 \mu\text{m}$ and $T_0 = 300$ K

Constant	Name	Value	Units
η	Refractive index	1.44963	
d_η/dT	Thermo-optic coefficient	8.7×10^{-6}	K^{-1}
k_T	Conductivity	1.38	W/m K
ϵ	Total spherical emissivity	0.90	
α_s	Bulk absorption coefficient	3.5×10^{-4}	m^{-1}
σ_s	Bulk scattering coefficient	0.5×10^{-4}	m^{-1}

have $\tau = 0.277$. The terms in these series are characterized by the roots of the equation

$$\zeta J_1(\zeta) - \tau J_0(\zeta) = 0, \quad (23)$$

which are reasonably well approximated by the zeros of $J_1(\zeta)$, $\zeta_k \cong (k + 1/4)\pi$ for $k \in \{0, 1, 2, \dots\}$, when $\tau < 1$.

The constants p_k are the coefficients of a Dini series expansion¹⁸ of the azimuthally symmetric incident intensity distribution $I(r)$, given by

$$I(r) \equiv \sum_k p_k J_0\left(\zeta_k \frac{r}{a}\right). \quad (24)$$

A straightforward calculation with Eq. (23) yields

$$p_k = \frac{2\zeta_k^2}{(\zeta_k^2 + \tau^2)J_0^2(\zeta_k)} \frac{1}{a^2} \int_0^a dr r J_0\left(\zeta_k \frac{r}{a}\right) I(r). \quad (25)$$

If we assume that the field is primarily made of the fundamental $\{00\}$ mode, then we can neglect the slight heating arising from higher-order modes. When the incident intensity describes a unit power TEM₀₀ Gaussian beam with spot radius w , we have $I(r) = (2/\pi w^2) \times \exp(-2r^2/w^2)$. Furthermore, if $w/a \ll 1$, we can extend the upper limit of integration in Eq. (25) to infinity, thereby obtaining the analytic expression

$$p_k = \frac{1}{\pi a^2} \frac{\zeta_k^2}{(\zeta_k^2 + \tau^2)J_0^2(\zeta_k)} \exp(-\beta_k), \quad (26)$$

where $\beta_k \equiv \frac{1}{8}(\zeta_k w/a)^2$.

The z dependence of the substrate temperature distribution given by Eq. (20) is typically very weak when $w/a \ll 1$, and the boundary conditions are radiative.¹⁸ In this case, near $r = 0$ we can use the identity $\sum_k p_k = I(0) = 2/\pi w^2$ to obtain the approximate temperature distribution $T_s(r) - T_s(0) \cong -(\alpha_p P_s/2\pi k_T)(r/w)^2$. In the thin-lens approximation, this quadratic temperature gradient yields a weak focal length²³

$$f = \frac{\pi w^2}{\alpha_s h P} \frac{k_T}{d_\eta/dT}, \quad (27)$$

where η is the refractive index of the substrate. The material constants for fused silica are shown in Table 1. For typical LIGO test masses, we have $w = 4$ cm, $h = 10$ cm, and $P = 500$ W, giving $f = 12$ km, a length only three times greater than that of a LIGO arm cavity.

The thermal load on the substrate causes a position-dependent phase shift across any wave front propagating

through the mirror. Defining the longitudinal optical path-difference (OPD) phase ϕ as

$$\phi(r) \equiv \frac{2\pi}{\lambda_0} \frac{d\eta}{dT} \int_{-h/2}^{h/2} dz T(r, z), \quad (28)$$

we obtain for the substrate and coating contributions

$$\begin{aligned} \phi_s(r) = P_s \frac{2\pi a^2}{\lambda_0 k_T} \frac{d\eta}{dT} \sum_k \frac{p_k}{\zeta_k^2} \\ \times \left[1 - \frac{2\tau A_k}{\gamma_k} \sinh(\gamma_k) \right] J_0 \left(\zeta_k \frac{r}{a} \right), \end{aligned} \quad (29a)$$

$$\phi_c(r) = P_c \frac{2\pi a^2}{\lambda_0 k_T} \frac{d\eta}{dT} \sum_k \frac{p_k}{\zeta_k} 2A_k \sinh(\gamma_k) J_0 \left(\zeta_k \frac{r}{a} \right), \quad (29b)$$

where $P_s \equiv \alpha_p h P$ and $P_c \equiv a_c P$ are the powers absorbed in the substrate and coating, respectively. If the thickness of the substrate is small compared with the wave-front radius of curvature, then we can approximate the propagator describing transmission through the substrate as a diffraction step through the aperture followed by a direct integration of the OPD across the aperture to describe the accumulated distortion. If we define the “edge-

$$\begin{aligned} \Phi_{s;mn,m'n'} = \frac{2\pi a^2}{\lambda_0 k_T} \frac{d\eta}{dT} \sum_k \frac{p_k}{\zeta_k^2} \left[1 - \frac{\tau}{\gamma_k} 2A_k \sinh(\gamma_k) \right] \\ \times \exp(-\beta_k) I_{k;mn,m'n'}, \end{aligned} \quad (31a)$$

$$\begin{aligned} \Phi_{c;mn,m'n'} = \frac{2\pi a^2}{\lambda_0 k_T} \frac{d\eta}{dT} \sum_k \frac{p_k}{\zeta_k} 2A_k \sinh(\gamma_k) \\ \times \exp(-\beta_k) I_{k;mn,m'n'}, \end{aligned} \quad (31b)$$

where we have defined the matrix integral I_k as

$$\begin{aligned} I_{k;mn,m'n'} \equiv \exp(\beta_k) \int \int_{-\infty}^{\infty} dx dy \left[J_0 \left(\zeta_k \frac{r}{a} \right) - 1 \right] \\ \times u_{m'n'}^\dagger(x, y) u_{mn}(x, y). \end{aligned} \quad (32)$$

Since the integrand is zero at $r = \sqrt{x^2 + y^2} = 0$, our definition of $\Delta\phi(r)$ allows us to explicitly ignore any phase shift accumulated due to the peak thermal change in the substrate refractive index, and instead we include only the contribution to the wave-front distortion arising from the *shape* of the temperature distribution. Using the same example Hermite–Gauss basis described in Subsection 2.B.1, for $m + n \leq 2$ and a given value of k , we obtain the square matrix elements

$$I_k(\beta_k) = \begin{bmatrix} 1 & 0 & 0 & -\frac{1}{\sqrt{2}}\beta_k & 0 & -\frac{1}{\sqrt{2}}\beta_k \\ 0 & 1 - \beta_k & 0 & 0 & 0 & 0 \\ 0 & 0 & 1 - \beta_k & 0 & 0 & 0 \\ -\frac{1}{\sqrt{2}}\beta_k & 0 & 0 & 1 - 2\beta_k + \frac{3}{4}\beta_k^2 & 0 & \frac{1}{4}\beta_k^2 \\ 0 & 0 & 0 & 0 & 1 - 2\beta_k + \frac{1}{2}\beta_k^2 & 0 \\ -\frac{1}{\sqrt{2}}\beta_k & 0 & 0 & \frac{1}{4}\beta_k^2 & 0 & 1 - 2\beta_k + \frac{3}{4}\beta_k^2 \end{bmatrix}. \quad (33)$$

to-center” OPD phase as $\Delta\phi(r) \equiv \phi(r) - \phi(0)$, then we can compute the total substrate thermal distortion matrix operator using

$$\begin{aligned} S_{mn,m'n'} = \int \int_{-\infty}^{\infty} dx dy \exp[i\Delta\phi(r)] \\ \times u_{mn}^\dagger(x, y) u_{m'n'}(x, y) \end{aligned} \quad (30)$$

for both substrate and coating absorption.

As we discussed above for the wave-front–mirror curvature matrix C given by Eq. (14), we seek a unitary approximation of the substrate thermal distortion matrix to ensure that power is conserved even when a finite set of unperturbed basis functions is used to compute the matrix elements. Once again, we begin by computing the matrix elements of the exponential arguments $\Delta\phi_s(r)$ and $\Delta\phi_c(r)$ (scaled to unit absorbed power) as, respectively,

Note that nonzero elements of $I_k(\beta_k)$ satisfy the relation $I_{k;mn,m'n'}(\beta_k) \approx O[\beta_k^{\frac{1}{2}(m+n+m'+n')}]$.

Collecting results, we can compute the net effective substrate OPD matrix operator in our unitary approximation as

$$S = \exp\{i[P_s\Phi_s + (P_h + P_a)\Phi_c]\}, \quad (34)$$

where P_s , P_h , and P_a are the total TEM₀₀ optical powers absorbed in the substrate, HR coating, and AR coating, respectively. The power distribution throughout the mirror volume is shown schematically in Fig. 4 for a dual-coated cylindrical mirror with substrate thickness h . A laser field F^+ is incident on the HR coating (the “front” of the mirror), and another field F^- is incident on the AR coating (the “back” of the mirror). Since we have assumed that the field primarily consists of the fundamen-

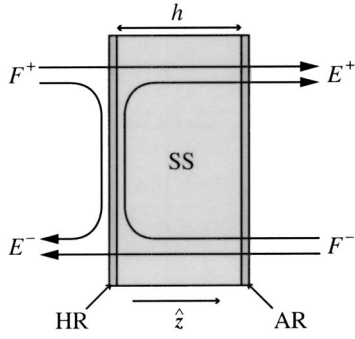


Fig. 4. Schematic diagram of field distributions in a mirror of thickness h , consisting of a substrate (SS) with applied high-reflectance (HR) and antireflecting (AR) coatings.

Table 2. Total Absorbed TEM₀₀ Powers for Each of the Three Regions Shown in Fig. 4, Summed Over the Lowest-Order Transverse Modes of all Active Sidebands

Region	Absorbed Power ^a
SS	$P_s = \alpha_s h \frac{1}{2} \sum_q (E_{00q}^+ ^2 + F_{00q}^- ^2)$
HR	$P_h = a_{hr} \frac{1}{2} \sum_q (F_{00q}^+ ^2 + F_{00q}^- ^2)$
AR	$P_a = a_{ar} \frac{1}{2} \sum_q (E_{00q}^+ ^2 + F_{00q}^- ^2)$

^a The factors of $\frac{1}{2}$ arise from our normalization convention for the laser electric field.

tal {00} mode, then the total power absorbed in the coatings and substrate depend only on the field amplitude expansion coefficients F_{00q} , as listed in Table 2. Here a_{hr} and a_{ar} are the dimensionless fractional power absorptions of the HR and AR coatings, respectively, and α_s is the power absorption coefficient of the substrate, with units of inverse length. The reflected field E^- is the superposition of the prompt reflection of F^+ and the residual of F^- that has been transmitted through the HR coating.

3. Transfer Matrix

We can extend our analysis of the reflection and transmission processes and build a general transfer matrix for fields incident on the mirror from either direction. First, we choose the laser-industry standard conventions for the phases of the amplitude reflection and transmission coefficients for a quarter-wave dielectric stack. Therefore the Maxwell boundary conditions for the HR coating generate the amplitude coefficients $-r$ for reflection and it for transmission, regardless of propagation direction. Losses in the HR coating due to absorption and scattering are included implicitly when $r^2 + t^2 < 1$. However, we must explicitly account for losses due to transmission through the substrate and AR coating using the amplitude coefficient

$$t_s = \exp[-(\alpha_s + \sigma_s)h/2] \sqrt{1 - (a_{ar} + s_{ar})}, \quad (35)$$

where σ_s is the scattering loss per unit length in the substrate, and s_{ar} is the scattering loss in the AR coating.

The propagator for reflection from the vacuum side of the HR is given by Eq. (9), and the resulting perturbation matrix for a mismatch between the radius of curvature of

the mirror and the wave front is given by Eq. (14) as $C(\gamma) \equiv C^-$. Since the propagator for reflection from the substrate side of the HR coating is also given by Eq. (9) with $-2/R_M \rightarrow 2n/R_M$,²³ where n is the refractive index of the substrate, the corresponding perturbation matrix is $C(-n\gamma) \equiv C^+$. Similarly, the propagator for transmission through the HR from the substrate to the vacuum is given by Eq. (14) with $-2/R_M \rightarrow (n-1)/R_M$,²³ so the transmission curvature mismatch matrix operator is $C[(n-1)\gamma/2] = (C^-C^+)^{1/2}$.

In Subsections 2.D.2 and 3.B, we will adjust the microscopic positions of some of the mirrors to ensure that the perturbed interferometers maintain the appropriate resonant phase conditions as the system evolves. If the mirror in Fig. 4 is moved in the positive \hat{z} direction (i.e., toward the right in the diagram) by the microdisplacement $\Delta z \lesssim \lambda$, then reflection from the “front” of the mirror introduces a relative phase $\exp(+i2k\Delta z)$, while reflection from the “back” of the mirror requires a phase adjustment of $\exp(-i2k\Delta z)$.

Collecting these results, the final mirror transfer matrix depicted in Fig. 5 is

$$\begin{bmatrix} E^- \\ E^+ \end{bmatrix} = \begin{bmatrix} T^- & R^- \\ R^+ & T^+ \end{bmatrix} \begin{bmatrix} F^+ \\ F^- \end{bmatrix}, \quad (36)$$

where the transmission operators are

$$T^- = itt_s(C^-C^+)^{1/2}SA, \quad (37a)$$

$$T^+ = itt_sS(C^+C^-)^{1/2}A, \quad (37b)$$

and the reflection operators are

$$R^- = -r \exp(+i2k\Delta z)C^-A, \quad (38a)$$

$$R^+ = -rt_s^2 \exp(-i2k\Delta z)SC^+SA. \quad (38b)$$

In the lossless case where $r^2 + t^2 = t_s^2 = 1$ and A is the identity matrix, the explicit unitarity of the C^+ , C^- , and S matrix operators guarantees that $|E^+|^2 + |E^-|^2 = |F^+|^2 + |F^-|^2$.

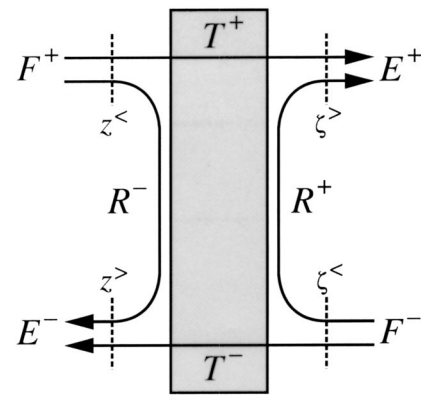


Fig. 5. Schematic diagram of the generalized mirror transfer matrix given by Eq. (36). The HR-coated surface of the mirror is on the left. The labels $z^<$ and $z^>$ denote the input and output reference planes, respectively, near the HR surface, while $\zeta^<$ and $\zeta^>$ are the input and output reference planes near the AR surface.

C. Beam Splitter

1. Aperture-Diffraction and Thermal-Focusing Operators

The analysis of the aperture-diffraction and thermal-focusing operators for the case of a 45° beam splitter is similar to that of a mirror. However, even though the beam splitter has the same cylindrically symmetric substrate as the mirror shown in Fig. 3, the nonnormal angle of incidence will require the elements of the perturbative matrix operators to be computed numerically. We will assume here that the HR-coated surface of the beam splitter is flat, allowing us to ignore both curvature mismatch and astigmatism when we build the transfer matrix in Subsection 2.C.2.

The aperture-diffraction operator for *reflection* from the HR-coated surface of the beam splitter is given by

$$A_{mn,m'n'} = \iint_{\mathcal{E}} dx dy u_{mn}^\dagger(x, y) u_{m'n'}(x, y), \quad (39)$$

where \mathcal{E} represents an elliptical aperture with semimajor (y) axis a and semiminor (x) axis $a/\sqrt{2}$. Strictly speaking, the diffraction operator for *transmission* through the substrate is more complicated than Eq. (39) because of refraction at each vacuum–dielectric interface, particularly since the effective clear aperture (in the horizontal plane) after propagation through the substrate has been reduced by the distance $h/2\eta$, or ~ 1.4 cm for LIGO. In principle, we can construct separate operators for reflective and transmissive aperture diffraction, but in practice we have found that the resulting effect on the recycled-power enhancement of the standard PRFPMI configuration shown in Fig. 1 was negligible. Hence in our simulations, we have made the simplifying approximation that Eq. (39) can be used to represent aperture-diffraction effects for both reflection and transmission.

The distribution of absorbed power within the beam-splitter volume is illustrated in Fig. 6, where we have introduced the primary propagation paths labeled parallel (\parallel) and perpendicular (\perp) relative to the propagation of the input laser field in Fig. 1. Following the conventions of Subsection 2.B.2 as closely as possible, we then label the input fields incident on the front (HR-coated) side of the mirror with $\text{sign}(\hat{\mathbf{k}} \cdot \hat{\mathbf{z}}) > 0$ as $F^{+\parallel}$ and $F^{+\perp}$, and those incident on the back (AR-coated) side of the mirror, with $\text{sign}(\hat{\mathbf{k}} \cdot \hat{\mathbf{z}}) < 0$ as $F^{-\parallel}$ and $F^{-\perp}$. Together with the four corresponding output fields shown in Fig. 6, these fields generate five distinct optical power absorption regions. The total TEM_{00} optical power absorbed in each of these regions is listed in Table 3, where $h' \equiv h/(1 - 1/2\eta^2)^{1/2}$ is the distance traveled through the substrate by the refracted beams.

Diffusion of heat from each of the optical absorption regions contributes to the total OPD distortion for both the parallel and perpendicular propagation paths. Following the conventions we established in Subsection 2.B.2 and Eqs. (31), for the *parallel* propagation path shown in Fig. 6, we denote the substrate OPD phase operators corresponding to the five absorption regions SS^\parallel , SS^\perp , HR, AR^\parallel , and AR^\perp as Φ_s^\parallel , Φ_s^\perp , Φ_c' , Φ_c^\parallel , and Φ_c^\perp , respectively. Since the perpendicular and parallel propagation paths are symmetric under reflection in the x – z plane about the

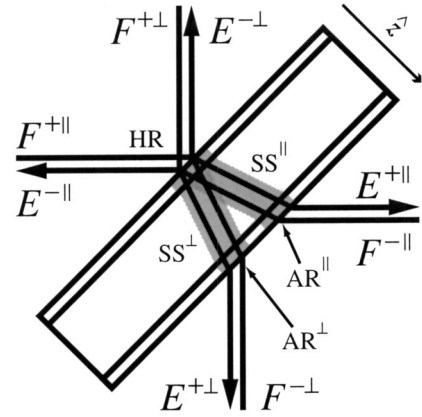


Fig. 6. Interaction of the two primary propagation paths, parallel (\parallel) and perpendicular (\perp), with the five optical absorption regions that cause thermal focusing in the beam-splitter substrate: SS^\parallel , SS^\perp , HR, AR^\parallel , and AR^\perp .

Table 3. Total Absorbed TEM_{00} Powers for Each of the Five Absorption Regions Shown in Fig. 6, Summed Over the Lowest-Order Transverse Modes of all Active Sidebands^a

Region	Absorbed Power
SS^\parallel	$P_s^\parallel = \alpha_s h' \frac{1}{2} \sum_q (E_{00q}^{+\parallel} ^2 + F_{00q}^{-\parallel} ^2)$
SS^\perp	$P_s^\perp = \alpha_s h' \frac{1}{2} \sum_q (E_{00q}^{+\perp} ^2 + F_{00q}^{-\perp} ^2)$
HR	$P_h = \alpha_{hr} \frac{1}{2} \sum_q (F_{00q}^{+\parallel} ^2 + F_{00q}^{+\perp} ^2 + F_{00q}^{-\parallel} ^2 + F_{00q}^{-\perp} ^2)$
AR^\parallel	$P_a^\parallel = \alpha_{ar} \frac{1}{2} \sum_q (E_{00q}^{+\parallel} ^2 + F_{00q}^{-\parallel} ^2)$
AR^\perp	$P_a^\perp = \alpha_{ar} \frac{1}{2} \sum_q (E_{00q}^{+\perp} ^2 + F_{00q}^{-\perp} ^2)$

^aThe factors of $\frac{1}{2}$ arise from our normalization convention for the laser electric field.

z axis, the same set of operators can be used to represent the substrate OPD distortion for perpendicular propagation, but in the order Φ_s^\perp , Φ_s^\parallel , Φ_c' , Φ_c^\perp , and Φ_c^\parallel . Hence in a particular basis, the net substrate thermal OPD matrix operators for the two propagation paths can be written with our unitary approximation as

$$S^\parallel = \exp\{i[P_s^\parallel \Phi_s^\parallel + P_s^\perp \Phi_s^\perp + P_h \Phi_c' + P_a^\parallel \Phi_c^\parallel + P_a^\perp \Phi_c^\perp]\}, \quad (40a)$$

$$S^\perp = \exp\{i[P_s^\parallel \Phi_s^\perp + P_s^\perp \Phi_s^\parallel + P_h \Phi_c' + P_a^\parallel \Phi_c^\perp + P_a^\perp \Phi_c^\parallel]\}. \quad (40b)$$

For the purposes of the initial LIGO simulations discussed in Subsection 3E, we first used finite-element software to compute the temperature distribution everywhere in the beam-splitter substrate due to absorption of 1 W of TEM_{00} optical power (choosing the initial LIGO spot size at the beam splitter) in each of the five regions shown in Fig. 6. Following the same basic approach as that of Subsection 2.B.2, we then computed the matrix elements of the five parallel OPD operators in Eq. (40) using a Hermite–Gauss basis having the same spot size. In our simulation runs, we simply scaled each matrix by the appropriate absorbed power and then computed S^\parallel and S^\perp by matrix exponentiation.

2. Transfer Matrix

As in the case of the mirror described in Subsection 2.B.3, we can construct a generalized transfer matrix for the beam splitter that includes the effects of aperturing, thermal focusing, and longitudinal microdisplacement. Once again, we adopt the industry-standard convention for the phases of the quarter-wave amplitude reflection and transmission coefficients of the HR coating, and we apply the substrate/AR amplitude transmission coefficient given by Eq. (35) with $h \rightarrow h'$. However, as shown in Subsection 2.E.2, the definition of the beam-splitter position is more subtle than that of the mirror: It consists of a static contribution z that represents the location chosen for the beam splitter when used in cold, unperturbed systems, and a dynamic contribution Δz that is used in heated interferometers to maintain a given intracavity phase condition. Hence if the beam splitter in Fig. 6 is displaced in the positive \hat{z} direction (i.e., away from the HR coating along the beam-splitter axis of cylindrical symmetry) by the total displacement $z + \Delta z$, then reflection from the “front” of the beam splitter introduces an additional relative phase $\exp[+i2\sqrt{2}k(z + \Delta z)]$, while reflection from the “back” of the beam splitter requires a phase adjustment $\exp[-i2\sqrt{2}k(z + \Delta z)]$.

Collecting these results, the final beam-splitter transfer matrix depicted in Fig. 7 is

$$\begin{bmatrix} E^{-\parallel} \\ E^{+\perp} \\ E^{+\parallel} \\ E^{-\perp} \end{bmatrix} = \begin{bmatrix} T^{-\parallel} & R^{-\parallel} & 0 & 0 \\ R^{+\perp} & T^{+\perp} & 0 & 0 \\ 0 & 0 & T^{+\parallel} & R^{+\parallel} \\ 0 & 0 & R^{-\perp} & T^{-\perp} \end{bmatrix} \begin{bmatrix} F^{-\parallel} \\ F^{+\perp} \\ F^{+\parallel} \\ F^{-\perp} \end{bmatrix}, \quad (41)$$

where, in the absence of curvature mismatch, the transmission operators are

$$T^{-\parallel} = T^{+\parallel} = itt'_s S^{\parallel} A, \quad (42a)$$

$$T^{-\perp} = T^{+\perp} = itt'_s S^{\perp} A, \quad (42b)$$

and the reflection operators are

$$R^{-\parallel} = R^{-\perp} = -r \exp[+i\sqrt{2}k(z + \Delta z)]A, \quad (43a)$$

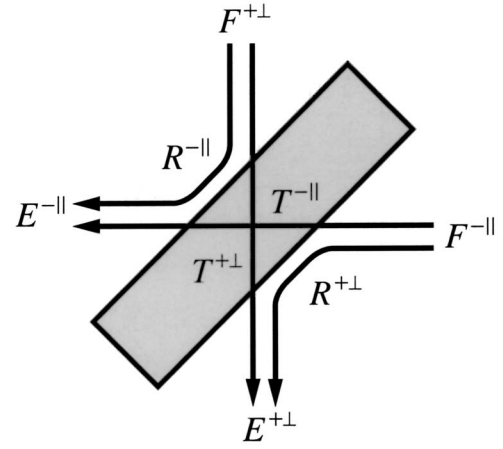
$$R^{+\parallel} = -rt_s'^2 \exp[-i\sqrt{2}k(z + \Delta z)]S^{\parallel} S^{\perp} A, \quad (43b)$$

$$R^{+\perp} = -rt_s'^2 \exp[-i\sqrt{2}k(z + \Delta z)]S^{\perp} S^{\parallel} A. \quad (43c)$$

In the lossless case where $r^2 + t^2 = t_s'^2 = 1$ and $A = 1$, the explicit unitarity of the S^{\parallel} and S^{\perp} matrix operators guarantees that $|E^{+\perp}|^2 + |E^{-\parallel}|^2 = |F^{+\perp}|^2 + |F^{-\parallel}|^2$ and $|E^{+\parallel}|^2 + |E^{-\perp}|^2 = |F^{+\parallel}|^2 + |F^{-\perp}|^2$.

D. Fabry–Perot Interferometers

The propagation schematic diagram of a Fabry–Perot interferometer (FPI) is shown in Fig. 8. The front (HR) input and output ports of mirror \mathcal{M}_1 and \mathcal{M}_3 are coupled through a propagation distance L_{13} . We can simplify later calculations of the optical performance of a power-recycled gravitational-wave interferometer if we first determine a transfer matrix for the FPI and then establish a procedure maintaining an optimum level of intracavity field amplitude enhancement in the presence of systematic perturbations. Although we develop the FPI transfer matrix in a basis-independent fashion and postpone



(a) Cross-coupling for $+$ \perp and $-$ \parallel

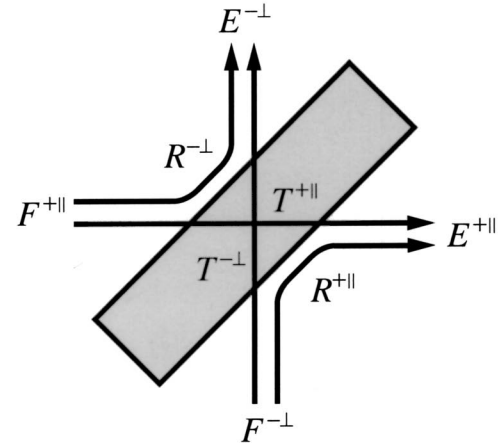


Fig. 7. Schematic diagram of the generalized beam-splitter transfer matrix given by Eq. (41). The HR surface of the mirror is on the upper left.

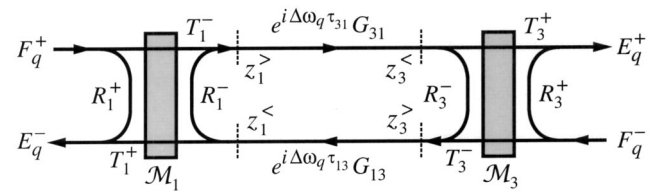


Fig. 8. Schematic diagram of the enhancement, reflection, and transmission operators of a Fabry–Perot interferometer, defined by Eq. (50), Eq. (55), and Eq. (56), respectively.

the discussion of the choice of an unperturbed basis set until we calculate steady-state fields in Subsection 3.C, we note that we will use the unperturbed Hermite–Gauss eigenmodes of one of the Fabry–Perot interferometers in Fig. 1 to develop a basis set for the entire gravitational-wave detector.

1. Transfer Matrix

Consider the schematic representation of the enhancement, reflection, and transmission operators of the Fabry–Perot interferometer shown in Fig. 8. If we express these operators using the transfer matrices of mir-

rors \mathcal{M}_1 and \mathcal{M}_3 , described in Subsection 2.B.3, then the self-consistent forward-propagation steps between the plane of incidence of \mathcal{M}_1 at $z_1^<$ and the plane of incidence of \mathcal{M}_3 at $z_3^>$ can be represented as

$$F_{1q}^- = \exp(i\Delta\omega_q\tau_{13})G_{13}(R_3^-F_{3q}^+ + T_3^-F_q^-), \quad (44a)$$

$$F_{3q}^+ = \exp(i\Delta\omega_q\tau_{31})G_{31}(R_1^-F_{1q}^- + T_1^-F_q^+), \quad (44b)$$

where F_q^+ is the amplitude of the external sideband field q incident on \mathcal{M}_1 , F_q^- is the amplitude of the external sideband field q incident on \mathcal{M}_3 , F_{1q}^- is the amplitude of frequency component q incident on reference plane $z_1^<$, and F_{3q}^+ is the corresponding field incident on reference plane $z_3^>$. Here G_{31} is the Gouy operator describing the forward propagation step from $z_1^>$ to $z_3^<$, while G_{13} is the corresponding operator describing propagation from $z_3^>$ to $z_1^<$. (In a power-orthonormal basis, the matrices representing these operators are identical.) If the length of the vacuum separating \mathcal{M}_1 from \mathcal{M}_3 is L_{31} , then the single-pass propagation time is $\tau_{31} = L_{31}/c = \tau_{13}$.

Using the concatenated column vectors $[E_{1q}^- \ E_{3q}^-]^T$ and $[F_q^- \ F_q^+]^T$, we can construct a system of sparse matrix equations that can be efficiently solved numerically by Gaussian elimination:

$$[1 - \hat{G}(\Delta\omega_q)\hat{R}^-] \begin{bmatrix} F_{1q}^- \\ F_{3q}^+ \end{bmatrix} = \hat{G}(\Delta\omega_q)\hat{T}^- \begin{bmatrix} F_q^- \\ F_q^+ \end{bmatrix}, \quad (45)$$

where

$$\hat{T}^- = \begin{bmatrix} T_3^- & 0 \\ 0 & T_1^- \end{bmatrix}, \quad \hat{R}^- = \begin{bmatrix} 0 & R_3^- \\ R_1^- & 0 \end{bmatrix}, \quad (46)$$

$$\hat{G}(\Delta\omega) = \begin{bmatrix} \exp(i\Delta\omega\tau_{13})G_{13} & 0 \\ 0 & \exp(i\Delta\omega\tau_{31})G_{31} \end{bmatrix}. \quad (47)$$

Alternatively, for a purely analytic calculation, we can define the global enhancement operator

$$\hat{H}(\Delta\omega) = [1 - \hat{G}(\Delta\omega)\hat{R}^-]^{-1}\hat{G}(\Delta\omega)\hat{T}^- \quad (48)$$

and then solve Eq. (45) analytically to obtain

$$\begin{bmatrix} F_{1q}^- \\ F_{3q}^+ \end{bmatrix} = \begin{bmatrix} H_1^-(\Delta\omega_q) & H_1^+(\Delta\omega_q) \\ H_3^-(\Delta\omega_q) & H_3^+(\Delta\omega_q) \end{bmatrix} \begin{bmatrix} F_q^- \\ F_q^+ \end{bmatrix}, \quad (49)$$

where the operators representing the enhancements at each of the reference planes in Fig. 8 are given by

$$H_1^-(\Delta\omega) = [1 - \exp(i2\Delta\omega\tau_{13})G_{13}R_3^-G_{31}R_1^-]^{-1} \times \exp(i\Delta\omega\tau_{13})G_{13}T_3^-, \quad (50a)$$

$$H_1^+(\Delta\omega) = [1 - \exp(i2\Delta\omega\tau_{13})G_{13}R_3^-G_{31}R_1^-]^{-1} \times \exp(i2\Delta\omega\tau_{13})G_{13}R_3^-G_{31}T_1^-, \quad (50b)$$

$$H_3^-(\Delta\omega) = [1 - \exp(i2\Delta\omega\tau_{31})G_{31}R_1^-G_{13}R_3^-]^{-1} \times \exp(i2\Delta\omega\tau_{31})G_{31}R_1^-G_{13}T_3^-, \quad (50c)$$

$$H_3^+(\Delta\omega) = [1 - \exp(i2\Delta\omega\tau_{31})G_{31}R_1^-G_{13}R_3^-]^{-1} \times \exp(i\Delta\omega\tau_{31})G_{31}T_1^-. \quad (50d)$$

From Fig. 8, we see that each of the output fields E_q^- and E_q^+ can be expressed as the sum of a prompt reflection

of the corresponding input field and an enhanced intracavity field transmitted through the adjacent mirror, giving

$$E_q^- = T_1^+F_{1q}^- + R_1^+F_q^+, \quad (51a)$$

$$E_q^+ = T_3^+F_{3q}^+ + R_3^+F_q^-, \quad (51b)$$

or, from Eq. (48) and Eq. (49),

$$\begin{bmatrix} E_q^- \\ E_q^+ \end{bmatrix} = [\hat{R}^+ + \hat{T}^+\hat{H}(\Delta\omega_q)] \begin{bmatrix} F_q^- \\ F_q^+ \end{bmatrix}, \quad (52)$$

where

$$\hat{T}^+ = \begin{bmatrix} T_1^+ & 0 \\ 0 & T_3^+ \end{bmatrix}, \quad \hat{R}^+ = \begin{bmatrix} 0 & R_1^+ \\ R_3^+ & 0 \end{bmatrix}. \quad (53)$$

We can now construct an explicit transfer matrix similar to Eq. (36) for the FPI as a monolithic optical element. With Fig. 5 as a guide, Eq. (52) gives

$$\begin{bmatrix} E_q^- \\ E_q^+ \end{bmatrix} = \begin{bmatrix} T_{\text{FPI}}^-(\Delta\omega_q) & R_{\text{FPI}}^-(\Delta\omega_q) \\ R_{\text{FPI}}^+(\Delta\omega_q) & T_{\text{FPI}}^+(\Delta\omega_q) \end{bmatrix} \begin{bmatrix} F_q^- \\ F_q^+ \end{bmatrix}, \quad (54)$$

where the transmission operators are

$$T_{\text{FPI}}^-(\Delta\omega) = T_1^+H_1^-(\Delta\omega), \quad (55a)$$

$$T_{\text{FPI}}^+(\Delta\omega) = T_3^+H_3^+(\Delta\omega), \quad (55b)$$

and the reflection operators are

$$R_{\text{FPI}}^-(\Delta\omega) = R_1^+ + T_1^+H_1^+(\Delta\omega), \quad (56a)$$

$$R_{\text{FPI}}^+(\Delta\omega) = R_3^+ + T_3^+H_3^-(\Delta\omega). \quad (56b)$$

2. Idealized Simulation of Servo-Controlled Resonator Length Locking

Suppose that the FPI has been initialized with a particular set of configuration parameters for mirrors \mathcal{M}_1 and \mathcal{M}_3 , the initial thermal loads are negligible, and the initial microdisplacements of both mirrors are set to zero. At some later time, a perturbation is introduced, such as a different curvature for \mathcal{M}_1 , that alters the resonance condition of the cavity. We assume that a biorthonormal set of unperturbed basis functions $u_{mn}(\mathbf{r})$ has been chosen to represent both the intracavity and extracavity transverse laser fields before any perturbations, and we wish to compute the corresponding perturbed transfer mirror matrix given by Eq. (36) in that unperturbed basis.

In any experiment that uses an FPI, the fields emerging from the resonator will be monitored and the cavity length will be adjusted to maintain optimum enhancement. However, rather than simulate a servo-mechanical control loop, we choose to compute a microdisplacement Δz_1 for \mathcal{M}_1 directly from a numerical determination of the net round-trip phase accumulated by the lowest-loss carrier eigenmode of the resonator. Beginning and ending at the reference plane $z_1^<$, the perturbed round-trip propagator at the carrier frequency for the FPI shown in Fig. 8 is

$$K_{\text{FPI}}(\Delta z_1) = \exp(-i2k\Delta z_1)G_{13}R_3^-G_{31}R_1^-, \quad (57)$$

where we have chosen to extract from Eq. (38a) the explicit phase offset arising from a nonzero value of Δz_1 .

We can then compute the spectrum of eigenvalues of $K_{\text{FPI}}(0)$ and select the eigenvalue $\lambda_0 \equiv |\lambda_0| \exp(i\phi_0)$ with the largest magnitude (i.e., the smallest round-trip loss). Clearly, the corresponding eigenvector E_0 is also an eigenvector of the matrix operator $K_{\text{FPI}}(\Delta z_1)$, with the eigenvalue $\lambda_1 = \lambda_0 \exp(-i2k\Delta z_1)$. Hence if we choose

$$\Delta z_1 = \frac{\phi_0}{2k}, \quad (58)$$

then the net round-trip phase accumulated by E_0 will be zero, and that mode will satisfy the resonance condition. In our simulations, we maintain a record of the most recently chosen lowest-loss eigenvector, and in the case of degeneracy we choose the eigenmode having the largest value of the inner product with the previous eigenvector.

Suppose that we have followed this procedure and computed the eigenvector E_0 of the matrix operator $K_{\text{FPI}}(\phi_0/2k)$, representing a maximally resonant field amplitude at reference plane $z_1^<$ in Fig. 8. We can mode match this field by choosing input fields that optimally couple to E_0 through the global enhancement operator $\hat{H}(0)$. For example, if we solve the matrix equation $E_0 = H_1^+(0)F_0^+$ for F_0^+ , where $H_1^+(0)$ is given by Eq. (50b), we obtain the intuitively self-consistent result

$$F_0^+ = \left(\frac{1 - |\lambda_0|}{\lambda_0^*} \right) (T_1^-)^{-1} R_1^- E_0. \quad (59)$$

A similar mode-matching condition for the back reference plane and incident field can be found by the same procedure.

E. Michelson Interferometer

The propagation schematic of a generalized Michelson interferometer (MI) is shown in Fig. 9. The back (AR) parallel input and output ports are coupled to either a mirror or FPI \mathcal{M}_I through a propagation distance L_{16} , and the front (HR) perpendicular ports are coupled to either a mirror or FPI \mathcal{M}_{II} through a propagation distance L_{26} . We can simplify later calculations of the optical performance of a power-recycled gravitational-wave interferometer if we first determine a transfer matrix for the MI and then establish a procedure for satisfying the dark-port condition in the presence of perturbations. As in Subsection 2.D, we develop the MI transfer matrix in a basis-independent fashion and postpone the discussion of the choice of an unperturbed basis set until we calculate steady-state fields in Subsection 3.C.

1. Transfer Matrix

By comparing Fig. 7 and Fig. 9, we can connect the MI input and output fields of frequency component q with the front parallel and back perpendicular fields of the beam splitter using the associations

$$E^{-||} \rightarrow E_q^-, \quad F^{-\perp} \rightarrow F_q^+,$$

$$E^{+\perp} \rightarrow E_q^+, \quad F^{+||} \rightarrow E_q^-.$$

As shown in Fig. 9, the back parallel fields are coupled through reflection from optical component \mathcal{M}_I , and the

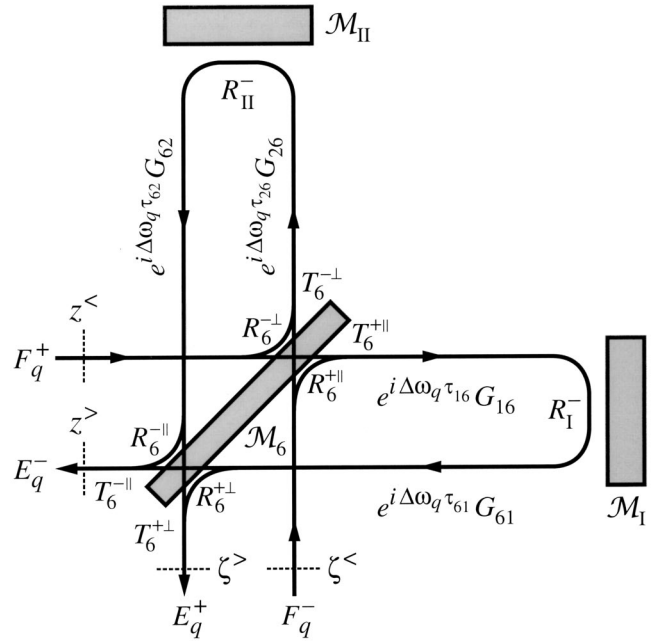


Fig. 9. Schematic diagram of the reflection and transmission operators of a Michelson interferometer, defined by Eq. (63). Note that the internal reflection operators $R_I^-(\Delta\omega_q)$ and $R_{II}^-(\Delta\omega_q)$ may each represent either the reflection operator of a mirror, given by Eq. (38a), or that of a Fabry–Perot interferometer, given by Eq. (56a). The labels $z^<$ and $z^>$ denote the input and output reference planes, respectively, near the HR surface of the beam splitter, while $\zeta^<$ and $\zeta^>$ are the input and output reference planes near the beam-splitter AR surface.

front perpendicular fields are coupled through reflection from \mathcal{M}_{II} . Therefore for frequency component q , we have

$$F_q^{-||} = K_{616}(\Delta\omega_q) E_q^{+||}, \quad (60a)$$

$$F_q^{+\perp} = K_{626}(\Delta\omega_q) E_q^{-\perp}, \quad (60b)$$

where

$$K_{616}(\Delta\omega) \equiv \exp(i2\Delta\omega\tau_{61}) G_{61} R_I^-(\Delta\omega) G_{16}, \quad (61a)$$

$$K_{626}(\Delta\omega) \equiv \exp(i2\Delta\omega\tau_{62}) G_{62} R_{II}^-(\Delta\omega) G_{26}. \quad (61b)$$

In Eq. (61a), G_{16} is the Gouy operator describing the forward-propagation step from the back parallel output port of the beam splitter \mathcal{M}_6 to the input port of \mathcal{M}_I , while G_{61} is the corresponding operator describing propagation from the output port of \mathcal{M}_I to the back parallel input port of \mathcal{M}_6 . If the length of the vacuum separating \mathcal{M}_6 from \mathcal{M}_I is L_{16} , then the single-pass propagation time is $\tau_{16} \equiv L_{16}/c = \tau_{61}$. In Eq. (61b), there is an equivalent set of propagation operators and times, with $1 \rightarrow 2$ and $I \rightarrow II$. The internal-reflection operators $R_I^-(\Delta\omega)$ and $R_{II}^-(\Delta\omega)$ may each represent either the reflection operator of a mirror, given by Eq. (38a), or that of a Fabry–Perot interferometer, given by Eq. (56a).

By substituting Eq. (60) into Eq. (41), we can immediately construct a transfer matrix similar to Eq. (36) for the MI as a monolithic optical element. Using Fig. 5 as a guide, we find

$$\begin{bmatrix} E_q^- \\ E_q^+ \end{bmatrix} = \begin{bmatrix} T_{\text{MI}}^-(\Delta\omega_q) & R_{\text{MI}}^-(\Delta\omega_q) \\ R_{\text{MI}}^+(\Delta\omega_q) & T_{\text{MI}}^+(\Delta\omega_q) \end{bmatrix} \begin{bmatrix} F_q^- \\ F_q^+ \end{bmatrix}, \quad (62)$$

where the individual reflection and transmission operators are defined by the matrix product

$$\begin{bmatrix} T_{\text{MI}}^-(\Delta\omega) & R_{\text{MI}}^-(\Delta\omega) \\ R_{\text{MI}}^+(\Delta\omega) & T_{\text{MI}}^+(\Delta\omega) \end{bmatrix} = \begin{bmatrix} T_6^{\parallel} & R_6^{\parallel} \\ R_6^{+\perp} & T_6^{+\perp} \end{bmatrix} \begin{bmatrix} K_{616}(\Delta\omega) & 0 \\ 0 & K_{626}(\Delta\omega) \end{bmatrix} \times \begin{bmatrix} T_6^{\parallel} & R_6^{\parallel} \\ R_6^{-\perp} & T_6^{-\perp} \end{bmatrix} \begin{bmatrix} 0 & 1 \\ 1 & 0 \end{bmatrix}. \quad (63)$$

2. Idealized Simulation of the Dark-Port Condition

Interferometric gravitational-wave Michelson interferometers typically operate with the beam splitter positioned so that the back perpendicular (antisymmetric) output port generates a dark fringe. In the model MI developed in the previous subsection, we can adjust the static position z_6 of the beam splitter to ensure that an unperturbed, mode-matched fundamental field (i.e., $\{m, n, q\} = \{0, 0, 0\}$) incident on the beam splitter's front parallel input port is canceled at the back perpendicular output port. Given our conventions for the phases of the amplitude reflection and transmission coefficients of a high-reflectance coating, we choose $z_6 = -\pi/2\sqrt{2}k$ ²² and obtain from Eq. (43)

$$R_6^{\parallel} = R_6^{\perp} = ir_6 \exp(+i\sqrt{2}k\Delta z_6)A_6, \quad (64a)$$

$$R_6^{+\parallel} = -ir_6 t_s'^2 \exp(-i\sqrt{2}k\Delta z_6)S_6^{\parallel}S_6^{\perp}A_6, \quad (64b)$$

$$R_6^{+\perp} = -ir_6 t_s'^2 \exp(-i\sqrt{2}k\Delta z_6)S_6^{\perp}S_6^{\parallel}A_6. \quad (64c)$$

If a compensation plate is placed in the vacuum between the beam splitter and \mathcal{M}_{II} , then (depending upon its orientation angle) it can be represented as either a mirror or a beam-splitter substrate with two antireflecting coatings and no curvature, and the corresponding operator can be inserted into the perpendicular propagator $K_{626}(\Delta\omega)$ given by Eq. (61b).

Suppose that the MI has been initialized with a particular set of configuration parameters, and in the absence of a thermal lens in any substrate, the dynamic microdisplacements of the beam splitter and the mirrors are set to zero. If the static beam-splitter position has been set to satisfy the dark-port condition for $q = 0$, then an unperturbed TEM₀₀ field incident on the front parallel port produces a vanishingly small output at the back perpendicular port. Insofar as it is possible, we wish to develop an algorithm that maintains this dark-port condition when the system has been perturbed.

Consider an arbitrary field F_0^+ incident on the front input port of the MI. At the back output port, the transmitted field can be found by simplifying Eq. (62) for $q = 0$, giving

$$E_0^+ = [D_1(\Delta z_6) + D_2(\Delta z_6)] F_0^+, \quad (65)$$

where we choose to extract from Eq. (64) the explicit phase offset arising from a nonzero value of Δz_6 , and write

$$D_1(\Delta z_6) = \exp(+i\sqrt{2}k\Delta z_6)R_6^{+\perp}K_{616}(0)T_6^{+\parallel}, \quad (66a)$$

$$D_2(\Delta z_6) = \exp(-i\sqrt{2}k\Delta z_6)T_6^{+\perp}K_{626}(0)R_6^{-\perp}. \quad (66b)$$

The corresponding power measured by a square-law detector at the dark port is therefore (within an additive constant)

$$\begin{aligned} P_0^+(\Delta z_6) &= \frac{1}{2}E_0^{+\dagger}E_0^+ \\ &= \frac{1}{2}F_0^{+\dagger}D_1^{\dagger}(\Delta z_6)D_2(\Delta z_6)F_0 + \text{c.c.} \\ &= |F_0^{+\dagger}D_1^{\dagger}(0)D_2(0)F_0| \cos(2\sqrt{2}k\Delta z_6 - \phi), \end{aligned} \quad (67)$$

where ϕ is the phase angle of $-F_0^{+\dagger}D_1^{\dagger}(0)D_2(0)F_0^+$. In order to minimize $P_0^+(\Delta z_6)$, we require that the condition $\partial P_0^+(\Delta z_6)/\partial \Delta z_6 = 0$ be satisfied, or

$$\Delta z_6 = \frac{\phi}{2\sqrt{2}k}. \quad (68)$$

We will incorporate this procedure into a general algorithm for simulating a servo-controlled resonator length-locking system for an entire gravitational-wave interferometer in Subsection 3.B.

3. POWER-RECYCLED FABRY-PEROT MICHELSON INTERFEROMETER

In previous sections, we have constructed the transfer matrices of the components needed to build a functionally complete description of a power-recycled Fabry-Perot Michelson interferometer (PRFPMI). The PRFPMI propagation schematic shown in Fig. 10 is a simplified form of the FPI schematic displayed in Fig. 8 and will allow us to determine the reduced transfer matrix with a minimum of calculation. In this case, the mirror \mathcal{M}_1 is replaced by the power-recycling mirror \mathcal{M}_5 , and the mirror \mathcal{M}_3 is replaced by the Michelson interferometer \mathcal{M}_{MI} . After determining the corresponding enhancement, reflection, and transmission operators of the PRFPMI, we develop a simulation of an idealized servo-controlled length-locking system that incorporates the dark-port condition algorithm described in Subsection 2.E.2. We then demonstrate the determination of a set of unper-

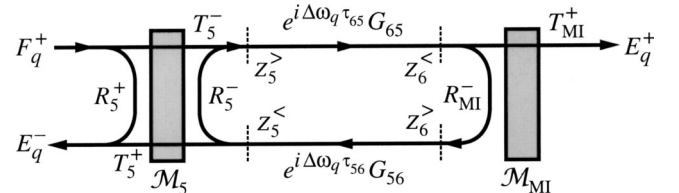


Fig. 10. Schematic diagram of the enhancement, reflection, and transmission operators of a power-recycled Fabry-Perot Michelson interferometer, defined by Eq. (70) and Eq. (72), respectively.

turbed basis functions that can be used to describe the electromagnetic intracavity and extracavity fields, and we develop a numerical algorithm for the computation of the steady-state fields under the influence of both geometric and thermal perturbations. After a detailed comparison of the predictions of this model with those of a fast-Fourier-transform code set in two important special cases, we evaluate the optical performance of the baseline LIGO design.

A. Transfer Matrix

Consider the schematic representation of the enhancement, reflection, and transmission operators of the interferometer shown in Fig. 10. If we express these operators using the transfer matrices of \mathcal{M}_1 and \mathcal{M}_{MI} , respectively described in Subsections 2.B.3 and 2.E.1, then the intracavity field enhancements can be represented as

$$F_{5q}^- = H_5^+(\Delta\omega_q)F_q^+, \quad (69a)$$

$$F_{6q}^+ = H_6^+(\Delta\omega_q)F_q^+, \quad (69b)$$

where F_q^+ is the amplitude of the external sideband field q incident on \mathcal{M}_5 , F_{5q}^- is the amplitude of frequency component q incident on reference plane $z_5^<$, and F_{6q}^+ is the corresponding field incident on reference plane $z_6^<$. By comparison with Eq. (44), the enhancement operators are

$$H_5^+(\Delta\omega) = [1 - \exp(i2\Delta\omega\tau_{56})G_{56}R_{\text{MI}}^-(\Delta\omega)G_{65}R_5^-]^{-1} \\ \times \exp(i2\Delta\omega\tau_{56})G_{56}R_{\text{MI}}^-(\Delta\omega)G_{65}T_5^-, \quad (70a)$$

$$H_6^+(\Delta\omega) = [1 - \exp(i2\Delta\omega\tau_{65})G_{65}R_5^-G_{56}R_{\text{MI}}^-(\Delta\omega)]^{-1} \\ \times \exp(i\Delta\omega\tau_{65})G_{65}T_5^-, \quad (70b)$$

where G_{65} is the Gouy operator describing the forward propagation step from $z_5^>$ to $z_6^<$, and G_{56} is the corresponding operator describing propagation from $z_6^>$ to $z_5^<$. If the length of the vacuum separating \mathcal{M}_5 from \mathcal{M}_{MI} is L_{65} , then the single-pass propagation time is $\tau_{65} \equiv L_{65}/c = \tau_{56}$. The front transmission and reflection operators of the power-recycling mirror, T_5^- and R_5^- , are given by Eq. (37a) and Eq. (38a), respectively. The front reflection operator of the MI, $R_{\text{MI}}^-(\Delta\omega)$, is given by the appropriate element of Eq. (63).

Given the PRFPMI schematic shown in Fig. 10 and the enhancement operators $H_5^+(\Delta\omega)$ and $H_6^+(\Delta\omega)$, we obtain the output fields E_q^- and E_q^+ as

$$E_q^- = R_{\text{IFO}}^-(\Delta\omega_q)F_q^+, \quad (71a)$$

$$E_q^+ = T_{\text{IFO}}^+(\Delta\omega_q)F_q^+, \quad (71b)$$

where the transmission and reflection operators are

$$T_{\text{IFO}}^+(\Delta\omega) = T_{\text{MI}}^+(\Delta\omega)H_6^+(\Delta\omega), \quad (72a)$$

$$R_{\text{IFO}}^-(\Delta\omega) = R_5^+ + T_5^+H_5^+(\Delta\omega). \quad (72b)$$

B. Idealized Simulation of Servo-Controlled Resonator Length Locking

Although the transfer-matrix schematics of the FPI and the PRFPMI, shown in Fig. 8 and Fig. 10, respectively, are similar, the resonant structure of the MI and the dark-port condition significantly complicate simulations

of an idealized resonator length-locking system. Clearly, we need to adjust the position of the power recycling mirror \mathcal{M}_5 to maintain a “round-trip” resonance condition, but the round trip must include both resonances in the Michelson arms and reflection from a beam splitter that has been infinitesimally displaced to force compliance with the Michelson dark-port condition. In fact, we again choose to compute a microdisplacement Δz_5 for \mathcal{M}_5 directly from a numerical determination of the net round-trip phase accumulated by the lowest-loss carrier eigenmode of the entire resonator. Beginning and ending at the reference plane $z_5^<$, the perturbed round-trip propagator at the carrier frequency for the PRFPMI shown in Fig. 10 is

$$K_{\text{IFO}}(\Delta z_5, \Delta z_6) = \exp(-i2k\Delta z_5)G_{56}[T_6^{\parallel}K_{616}(0)T_6^{\parallel} \\ + \exp(-i2\sqrt{2}k\Delta z_6)R_6^{\parallel}K_{626}(0)R_6^{\perp}] \\ \times G_{65}R_5^-, \quad (73)$$

where we have chosen to extract from Eq. (38a) and Eq. (64a) the explicit phase offsets arising from nonzero values of Δz_5 and Δz_6 , respectively.

A close examination of Eq. (73) reveals that we can separate the idealized servo-locking algorithm into three consecutive stages, each with its own optimization process:

1. We follow the procedure described in Subsection 2.D.2 to adjust individually the positions of \mathcal{M}_1 and \mathcal{M}_2 to maximize the round-trip enhancement for the lowest-loss carrier eigenmode of each FPI.
2. We select an initial value for Δz_6 , and then compute the carrier eigenvalue spectrum of $K_{\text{IFO}}(0, \Delta z_6)$ to find both the eigenvalue λ_0 with the largest magnitude and the corresponding lowest-loss eigenvector E_0 . We set the Michelson input field $F_0^+ = G_{65}R_5^-E_0$ in Eq. (67), and then use Eq. (68) and the discussion in Subsection 2.E.2 to compute the new beam-splitter position $\Delta z_6'$ that satisfies the dark-port condition for E_0 . Since E_0 is generally *not* an eigenvector of $K_{\text{IFO}}(0, \Delta z_6')$, we iterate this step to determine an eigenvector E_0' and a beam-splitter displacement $\Delta z_6'$ such that successive values of the largest-magnitude eigenvalue $|\lambda_0'|$ differ by no more than a suitably small convergence threshold (typically 10^{-12} in our simulations).
3. As in the case of the FPI discussed in Subsection 2.D.2, the eigenvector E_0' is also an eigenvector of the matrix operator $K_{\text{IFO}}(\Delta z_5, \Delta z_6')$, with the eigenvalue $\lambda_5 = |\lambda_0'| \exp[i(\phi_0' - 2k\Delta z_5)]$. Hence if we choose

$$\Delta z_5 = \frac{\phi_0'}{2k}, \quad (74)$$

then the net round-trip phase accumulated by E_0' will be zero, and that mode will satisfy the resonance condition.

As in the case of the FPI, in our simulations we maintain a record of the most recently chosen lowest-loss eigenvec-

tor, and in the case of degeneracy we choose the eigenmode having the largest value of the inner product with the previous eigenvector.

Suppose that we have followed this procedure and computed the eigenvector E'_0 of the matrix operator $K_{\text{IFO}}(\phi'_0/2k, \Delta z'_0)$, representing a maximally resonant field amplitude at reference plane z'_5 in Fig. 10. We can mode match this field by choosing an input field that optimally couples to E_0 through the enhancement operator given by Eq. (70a). If we solve the matrix equation $E_0 = H_5^+(0) F_0^+$ for F_0^+ , we obtain

$$F_0^+ = \left(\frac{1 - |\lambda_0|}{\lambda_0^*} \right) (T_5^-)^{-1} R_5^- E_0, \quad (75)$$

in agreement with Eq. (59).

C. Computation of Steady-State Fields

In previous subsections, we have been largely unconcerned with the basis chosen to represent the operators that comprise the transfer matrices of the optical elements of the gravitational-wave interferometer. Instead, we have focused on the details of specifying the operator algebra needed to describe the physics of mirror perturbations. In this subsection, we intend to define a computational algorithm that will allow us to determine the self-consistent steady-state fields everywhere in a realistic model of a thermally loaded interferometer. We begin by describing a procedure to define an unperturbed transverse spatial basis that can be used to represent all intracavity and extracavity electromagnetic fields, and then we specify the initialization process we have used to prepare the computational model for perturbations. Finally, we present the simple iterative steady-state solution algorithm we have used to obtain convergence from the complete set of nonlinear coupled propagation equations describing the PRFPMI intracavity fields.

In the Michelson interferometer, the beam splitter couples two optical systems (each consisting of a vacuum region followed by either a mirror or a Fabry–Perot interferometer) that may have significantly different mode-matching requirements relative to some common reference plane. In principle, the determination of a set of eigenmodes that is common to both optical systems is a tedious numerical exercise, particularly in the context of the power-recycling scheme shown in Fig. 1. However, in practice, our simulations do not require the identification of an *ab initio* set of common eigenmodes. Rather, we seek a collection of self-consistent unperturbed basis functions capable of accurately representing the transverse spatial features of the laser field anywhere in the gravitational-wave interferometer. As we show here, these basis functions can be eigenmodes of the unperturbed parallel FPI *only*, propagated *unidirectionally* throughout the entire system.

Referring to Fig. 1, Fig. 8, and Fig. 9, we begin by ignoring all apertures everywhere in the system, and choosing the length and mirror curvatures of the unperturbed (e.g., infinite-aperture, spherical-mirror, and cold) parallel FPI. These geometric configuration parameters define a set of standing-wave eigenmodes with a particular spot size and a wave-front radius of curvature at \mathcal{M}_1 that

matches that of \mathcal{M}_1 before thermal loading. We select these eigenmodes as the spatial basis functions that will describe the transverse laser field everywhere in the system.

Referring to Fig. 1 and Fig. 10, we position another mirror at the location of the power recycling mirror (PRM) \mathcal{M}_5 to couple optically the two Fabry–Perot interferometers, and we propagate the lowest-loss (i.e., “fundamental”) basis function out of the parallel FPI through the beam splitter to the intracavity input reference plane $z_5^<$ of the PRM. We calculate the value of the curvature $1/R_F$ of the extracted fundamental FPI eigenmode at $z_5^<$ and set the unperturbed curvature of \mathcal{M}_5 to that value. We also compute the spot radius w_5 of the fundamental basis function at $z_5^<$ so that we can determine the perturbed curvature mismatch matrices C_5^\pm using the true curvature $1/R_5$ in Eq. (14) and Eq. (15).

Following the same unidirectional approach, we propagate the fundamental basis function from the PRM intracavity output reference plane $z_5^>$ to the intracavity reference planes $z_2^>$ of \mathcal{M}_2 and then $z_4^>$ of \mathcal{M}_4 in the perpendicular FPI. At each of these two reference planes, we compute the curvature and spot radius of the corresponding laser field and then set these values as the appropriate unperturbed parameters of these mirrors. As in the case of \mathcal{M}_5 , any discrepancies between the unperturbed curvatures of the propagated basis functions and the true curvatures of the perpendicular mirrors are then captured by the C^\pm perturbation matrices defined by Eq. (14).

We complete our specification of the unperturbed geometry of the interferometer by propagating a selected set of unperturbed transverse spatial eigenmodes from the parallel FPI throughout the PRFPMI. This procedure defines a (possibly incomplete) set of spatial basis functions with which intracavity fields in the PRFPMI can be specified. Furthermore, by propagating the intracavity basis functions out through both the dark port and \mathcal{M}_5 , we can use the same unperturbed basis for the extracavity fields F^+ , E^+ , and E^- shown in Fig. 10. In general, the input field F^+ will not be described solely by the outward-propagated fundamental eigenmode of the parallel FPI; instead, it will be represented by a linear combination of some subset of the modes available in the unperturbed basis.

The spherical-mirror, infinite-aperture, cold approximation of the unperturbed gravitational-wave interferometer lends itself to a convenient representation of intracavity fields by power-orthogonal Hermite–Gauss modes. However, even when the mirrors remain spherical and thermal lensing is ignored, this basis cannot represent all possible perturbed fields with arbitrarily high accuracy under all circumstances. For example, in cases where either the recycling cavity is geometrically unstable or a thermal lens is so strong that the sign of the curvature of a wave front propagating through the substrate changes, then we expect that the number of stable unperturbed basis functions needed to represent that field will become prohibitively large. Furthermore, if either finite apertures or nonspherical mirrors are used to define the unperturbed basis numerically, it is possible that residual diffraction of a non-Hermite–Gauss fundamental basis

function from \mathcal{M}_5 (followed by propagation to \mathcal{M}_6) will generate a field profile that has a mean spot radius that differs from the value computed with the field profile obtained by propagating the lowest-loss parallel eigenmode from \mathcal{M}_1 to \mathcal{M}_6 . In this case, a biorthogonal basis can be chosen, but special care must be taken to ensure that the eigenmode expansions converge.²⁵ When a self-consistent basis can be chosen, and the corresponding perturbation expansion of the physical observables under simulation converges, the matrix representation of the problem can allow computations that are orders of magnitude faster than those performed by FFT codes.

Now that we have defined a self-consistent set of spatial basis functions at every reference plane in the LIGO PRFPMI, we can introduce the perturbations by setting the apertures and curvatures of the mirrors and beam splitter to their true values, and then computing the matrices that characterize the effects of aperture diffraction, wave-front-mirror curvature mismatch, and thermal focusing on laser fields expressed as linear combinations of the *unperturbed* basis functions. Initially, we solve Eq. (69a) in the limit $F^+ \rightarrow 0$ to obtain the perturbed fields of the cold interferometer, and then we choose a relatively low but finite input power (e.g., 0.1 W) for the input field. The steady-state intracavity fields under this small thermal load can be found by a straightforward, self-consistent procedure:

1. Using the current intracavity fields, we compute the powers absorbed in the mirror and beam-splitter substrates and coatings, and we update the substrate thermal OPD matrix elements given by Eq. (34) and Eq. (40), which depend nonlinearly on these powers.
2. Following the procedure outlined in Subsection 3.B, we adjust the micropositions of \mathcal{M}_1 , \mathcal{M}_2 , \mathcal{M}_6 , and \mathcal{M}_5 to achieve optimum resonant phase conditions for the lowest-order carrier mode in each of the three optical cavities.
3. We recompute the intracavity fields using Eq. (69a).
4. We repeat the previous steps until the recycled power $\frac{1}{2} \sum_q |E_{5q}^-|^2$ has stabilized.

Note that we do *not* propagate the field from one reference plane to another throughout the interferometer. In this case, even when the simulated phase-control system is used, the fields tend to converge after a number of iterations implied by the photon storage lifetimes of the arm cavities. Furthermore, we do not use more complicated nonlinear gradient-search methods to determine the intracavity fields because the number of variables (field basis function coefficients) is extremely large, and the variables at any single location in the interferometer are linked to those at all other locations by nontrivial round-trip propagators. Instead, the solution procedure we have detailed above can provide convergence to a few parts in 10^4 in only a few iterations.

The steady-state fields arising from higher input powers can be found by initializing the convergence process with scaled field amplitudes computed at a lower power. For example, if a stable solution has been found at 2 W total input power, then the *same* collection of intracavity fields, scaled by a factor of 2, would be reasonable initial

values for an input power of 8 W. Similarly, if the input power is held constant, but some other parameter of the PRFPMI configuration (such as the PRM curvature) is varied, the intracavity fields can be reused from one parameter value to the next. In this way, a set of solutions for a variety of different interferometer parameter sets can be constructed in a few minutes with a typical desktop computer.

An object-oriented numerical computer model of the initial LIGO interferometer based on these algorithms has been implemented with the class mechanism of the MATLAB programming language.²⁶ The resulting collection of MATLAB source code files, hereafter referred to as “Melody,” is available publicly for examination and execution.²⁷

D. Comparison with a Fast-Fourier-Transform Model

In certain limited cases, the predictions made by Melody can be compared with those of a Fortran implementation of a fast-Fourier-transform (FFT) model of the initial LIGO interferometer.¹⁷ The FFT model was designed to investigate geometric requirements and tolerances for initial LIGO optical components, and it allows either a measured or simulated static OPD phase map to be included in each reflective surface. By contrast, the Melody solution method described in Subsection 3.C allows the evolving fields everywhere in the interferometer to alter the local phase maps with nonlinear thermal lensing, so that both the field and mirror are distorted by their reciprocal interaction. For the FFT, the paraxial approximation is used in order to calculate the propagators between mirrors, as matrix operators in the spatial frequency domain. The lengths are optimized in order to achieve a stationary locked configuration, and the power stored inside the arms and the recycling cavity is evaluated. The final fields obtained may be analyzed for modal composition. In contrast, the Melody program starts with a fixed number of paraxial modes. The matrix elements coupling the modes are then analytically calculated with the algorithms described in Subsections 2.B and 2.C, with the thermal effects perturbatively evaluated at every iteration until stationarity is achieved.

While the basic optics and wave-equation assumptions are the same, the two programs have markedly different implementations. In the case of the FFT code, the carrier and the sidebands are simulated by two separate, consecutive runs so that the cavity lengths are optimized for the carrier, and the dimensions of the recycling cavity are optimized for the sidebands. As discussed previously, the idealized Melody control system sets the cavity lengths by ensuring a round-trip phase of zero for the lowest-loss eigenmode. The FFT solutions scale linearly with initial field power, but in Melody, the power is shared by carrier and sidebands; the carrier and sideband fields are separately calculated, and their combined power at each iteration affects the thermal-lens distortion nonlinearly. The FFT features fine-grained meshing of fixed phase map information, being intended primarily to study arbitrary mirror aberrations. On the other hand, Melody is intended to much more rapidly study coarser-grained effects with specific emphasis on the nonlinear effects of thermal focusing. Significantly, the computational hard-

ware requirements for the codes are dramatically different: a typical FFT run requires 30–60 min. on a supercomputer, while a typical Melody computation requires only a few seconds to stabilize.

The parameters that we used in our simulations are shown in Table 4 and Table 5. The RF modulation frequency was chosen to be $\omega_1/2\pi = 24.485446$ MHz (with a modulation depth of 0.47), and the length of each arm cavity was adjusted slightly from the nominal value of 4000 m in the Melody computations to guarantee an antiresonance to within machine precision. The current design value of the initial LIGO common length (the average of the distances between the power-recycling mirror and the input test masses) is 9.183 m, and the differential length (or “Schnupp”) asymmetry (the difference between the distances between the parallel and perpendicular ITM and the PRM) is $L_S = 0.3$ m. The distance between the beam splitter and the PRM has the value 6.25 m, and all simulations were performed with the Nd:YAG laser wavelength $\lambda_0 = 1.0642$ μm . As a first comparison, both codes were used to simulate the unperturbed initial LIGO interferometer, with perfect mode matching, infinite-diameter optics, and no thermal distortion. The agreements between computations of reflected and transmitted power with analytical calculations are within 0.2% for both the FFT code and Melody.

In the absence of thermal loading, we have studied the dependence of the parallel (in-line) arm-cavity power buildup on the diameter of the ETM \mathcal{M}_3 . A comparison between the predictions of Melody and the FFT code tests the suitability of the former’s basis-function-expansion approach to calculating interferometer power levels, particularly when the cavity losses are large enough to re-

Table 4. High-Reflection (hr) and Antireflection (ar) Loss Parameters for the Initial LIGO Optical Elements Used in Our Simulations^{28 a}

Parameter	Loss (ppm)
a_{hr}	0.5
a_{ar}	0.5
s_{hr}	55.0
s_{ar}	90.0

^aWe assign a scattering loss of 900 ppm to the AR coatings of the ITM mirrors to account for power pick-off monitoring losses. Here a_e is the optical power absorption that contributes to the substrate thermal loss, and s_e is the scattering loss.

Table 5. Physical Parameters for the Initial LIGO Optical Elements Used in Our Simulations^{28 a}

Mirror	R_M (m)	h (m)	r^2	t^2
$\mathcal{M}_1, \mathcal{M}_2$	14 571.0	0.10	0.971	$1 - r^2 - l_{\text{hr}}$
$\mathcal{M}_3, \mathcal{M}_4$	7 400.0	0.10	$1 - t^2 - l_{\text{hr}}$	1.5×10^{-5}
\mathcal{M}_5	9 999.8	0.10	0.973	$1 - r^2 - l_{\text{hr}}$
\mathcal{M}_6	∞	0.04	0.495	$1 - r^2 - l_{\text{hr}}$

^aEach substrate is fused silica, with parameters given by Table 1 and a radius $a = 12.5$ cm. Here the total loss $l_{\text{hr}} = a_{\text{hr}} + s_{\text{hr}}$, where a_{hr} and s_{hr} are the power absorption and scattering losses in the high-reflection coating, respectively.

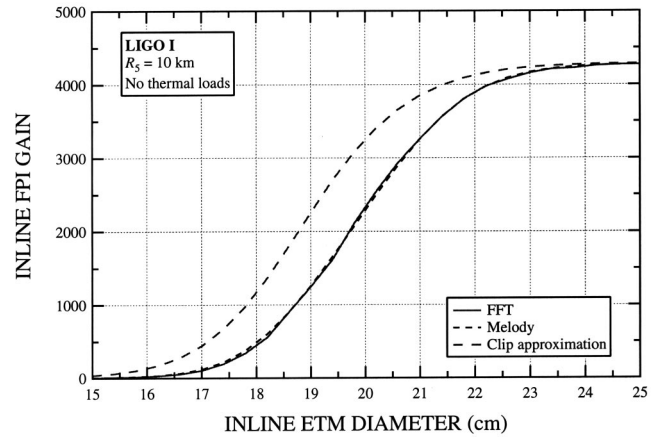


Fig. 11. Comparison between the predictions of computer code based on our model (Melody) and those of the FFT model in the case of simple aperturing. The power enhancement (or “gain”) at the parallel/in-line FPI reference plane z_1^+ in Fig. 8 is plotted as a function of the aperture of \mathcal{M}_3 . The “clip approximation” represents the result expected by assuming that the loss arises from simple single-pass aperture clipping at \mathcal{M}_3 .

quire the inclusion of a large number of modes. In Fig. 11, we plot the ratio of the total circulating optical power at reference plane z_1^+ in Fig. 8 to the total carrier input power $\frac{1}{2}|F_0^+|^2$. When the 28 lowest-loss Hermite–Gauss modes (corresponding to $m + n \leq 6$) of the parallel FPI are used, the agreement is excellent even at an ETM diameter of only 15 cm, which imposes a round-trip diffractive loss of approximately 2000 ppm. For comparison, we have included a trace displaying the stored power in the parallel arm expected when the intracavity loss is due to simple single-pass aperture clipping. Note that this naive assumption underestimates the true diffractive loss by a factor of ~ 2.14 for this beam spot size at \mathcal{M}_3 .

In the thermally loaded simulations that are described in Subsection 3.E, the increase in thermal focusing power of the ITM substrates improves the geometric stability of the power recycling cavity by increasing the apparent ITM radii of curvatures. However, if we reduce the radius of curvature (ROC) of either ITM below the design value of 14.571 km, the recycling cavity becomes unstable, resulting in a large reduction in stored power. Previous studies of this phenomenon using the FFT code have shown that, for small changes in ITM curvature, only the sidebands suffer this power degradation; the carrier resonance condition in the corresponding arm cavity serves to stabilize the recycling cavity mode by attenuating the antiresonant higher-order modes. Therefore since our model uses stable resonator eigenmodes as the spatial basis functions for the field expansions, this is a much more strenuous test than the aperture-reduction example, requiring a substantially greater number of transverse modes. In Fig. 12, we show the dependence of the power-recycling cavity gain on the perpendicular (outline) ITM radius of curvature. The Melody results for the carrier agree essentially perfectly with those of the FFT code even when we employ only the 28 lowest-loss Hermite–Gauss modes of the parallel FPI. However, to obtain reasonably small discrepancies between the predictions of the sideband behavior in the highly unstable

regime, we must include all basis functions satisfying $m + n \leq 20$, or 231 modes.

E. Initial LIGO Optical Performance Simulations

We now turn to simulations of the basic initial LIGO interferometer in the presence of thermal loading of the optics. Because of the high power levels maintained in the interferometer to suppress shot noise, the absorption of power in the ITM substrates and coatings and the subsequent thermal focusing must be incorporated into the interferometer design. Using Melody, we explore in detail the effects of this focusing on the optical performance of the interferometer. Since the recycling cavity is operating in a region of geometric stability under full thermal load, we have run our simulations using the 28 lowest-loss Hermite–Gauss modes (corresponding to $m + n \leq 6$) of the parallel FPI.

If the radius of curvature of the power-recycling mirror M_5 is chosen to be the cold-cavity mode-matched value shown in Table 5, the thermal distortions caused by the substrates in the recycling cavity will destroy this mode matching and significantly reduce the available recycling gain for the sidebands. In Fig. 13 and Fig. 14, we plot the sideband recycled powers $|F_{5,\pm 1}^-|^2$ given by Eq. (69a) as a function of the PRM ROC R_5 for the initial LIGO TEM₀₀ operating input laser power of 6.5 W, with 5.8 W delivered by the carrier when the sideband modulation depth is 0.47. (The feature near 11.5 km corresponds to the ROC at which the carrier TEM₀₀ emerging from the dark port is absolutely minimized by the pseudolocker.) The presence of the arm cavities significantly reduces the sensitivity of the carrier to these perturbations, resulting in an approximately constant recycling gain of 50 when the parameters specified in Table 1, Table 4, and Table 5 are used. Note that the optimum mode matching of the parallel and perpendicular segments of the recycling cavity occurs when the PRM ROC has increased to approximately 12.5 km.

One of the most striking details of Fig. 13 and Fig. 14 is the significant difference in the recycling gain of the

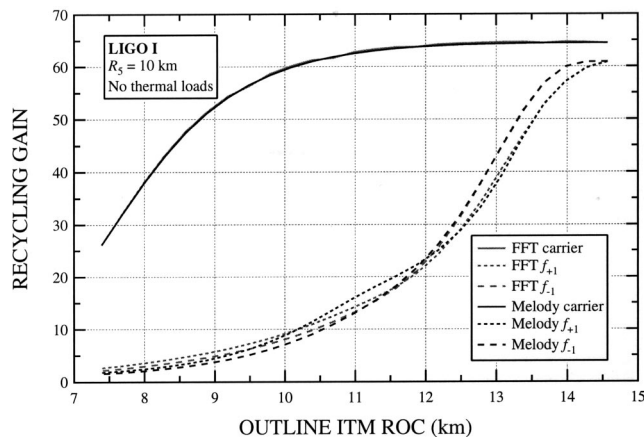


Fig. 12. Comparison between the predictions of Melody and those of the FFT model in the case of unstable curvature reduction. The gain at the recycling mirror reference plane $z_5^>$ in Fig. 10 is plotted as a function of the curvature of M_2 . Note that, in the absence of thermal loading, the recycling cavity becomes unstable for the resonant sidebands at a radius of curvature of 14480 m.

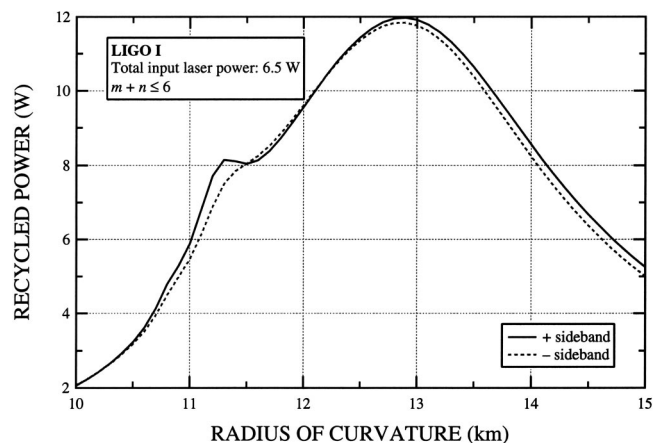


Fig. 13. Initial LIGO recycled powers as a function of the PRM radius of curvature. The total TEM₀₀ input laser power is 6.5 W, with 5.8 W delivered by the carrier.

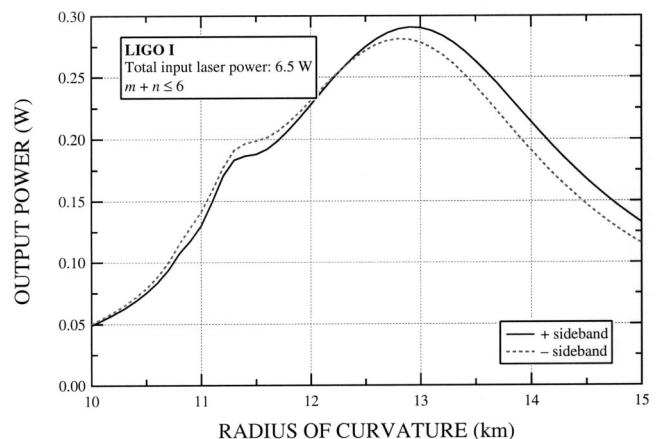


Fig. 14. Initial LIGO antisymmetric (“dark”) port output powers as a function of the PRM radius of curvature. The total TEM₀₀ input laser power is 6.5 W, with 5.8 W delivered by the carrier.

upper ($+\Delta\omega_1$) and lower ($-\Delta\omega_1$) sideband fields. Such a sideband imbalance can lead to significant gravitational-wave detection noise signatures that are qualitatively absent when the balance is exact. Since the ratio $\Delta\omega_1/\omega_0$ is immeasurably small for RF sidebands and (by design) there is a very high degree of geometrical symmetry between the Michelson branches of the interferometer, we naively expect the sideband fields to interact identically with geometrical distortions as long as these distortions are frequency independent at the RF scale. In principle, this symmetry is broken only by the macroscopic value of the Schnupp asymmetry $L_S \equiv L_{51} - L_{52}$, where L_{5j} is the optical path length separating M_5 and M_j . For gravitational-wave interferometers, L_S is much smaller than the Rayleigh length, so both sidebands should interact nearly identically with either arm, except for a phase accumulation proportional to the distortion-independent factor $\Delta\omega_1 L_S$.

In practice, however, the symmetry is also broken slightly by small differences between the mirror figures and loss parameters in the two Fabry–Perot resonators and much more significantly by the beam-splitter thermal lens in the parallel arm. Using both Melody and the FFT code, we have determined that our simulations strictly

show excellent sideband balance if either $L_S \rightarrow 0$ or the net branch distortions are identical. Of course, with Melody, we have determined that the branch distortions *cannot* be identical when the thermal lens in the beam-splitter substrate is significant; this source of additional distortion in the parallel arm requires a significant displacement of the beam splitter to maintain the dark-port condition and is therefore the primary cause of the imbalance shown in Fig. 13 and Fig. 14. In fact, as seen in Fig. 12, the FFT code reproduces this behavior when the field-mirror curvature mismatch at the perpendicular ITM becomes large, causing a significant difference between the net distortions of the two arms. Physically, the imbalance arises whenever the spatial structures of the sideband fields returning to the *front* of the beam splitter from the arms differ significantly, because the pseudolocker cannot adjust the positions of the beam splitter and power-recycling mirror to simultaneously optimize the carrier TEM_{00} performance *and* reduce dissimilarities between the sideband spatial field distributions.

Further studies with Melody have shown that it is possible to improve the sideband balance by adopting one of the following procedures:

1. As shown in Fig. 14, we can specify the curvature of the PRM to operate the system at a reduced average output power where the sideband balance is improved.
2. We can supplement the procedure outlined in Subsection 3.B with an additional step that readjusts the positions of both M_5 and M_6 , but at the expense of increasing the TEM_{00} carrier output power at the antisymmetric port by approximately an order of magnitude.

Both choices are nontrivial to execute in practice. The former requires a precise foreknowledge of the optical loss and geometric parameters of each of the optical components, and the latter choice adds considerable complexity to the servo-control system of the PRFPMI.

For the purposes of our discussion here, we have chosen a value of the PRM ROC that minimizes both the fundamental carrier power and the sideband imbalance at the antisymmetric output port. This strategy produces the optimum initial LIGO PRM radius of curvature as a function of total TEM_{00} input laser power shown in Fig.

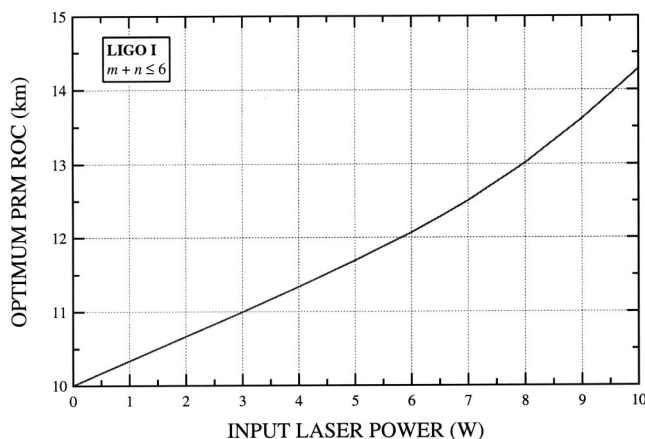


Fig. 15. Optimum initial LIGO PRM radius of curvature as a function of total TEM_{00} input laser power.

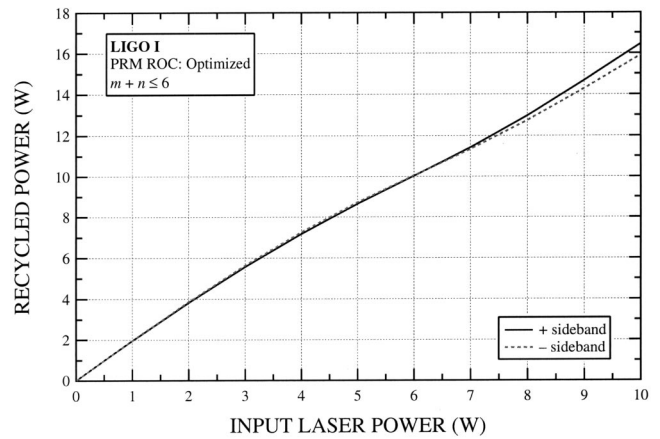


Fig. 16. Optimized initial LIGO recycled sideband powers as a function of total TEM_{00} input laser power. At each value of the input power, the PRM radius of curvature shown in Fig. 15 has been used.

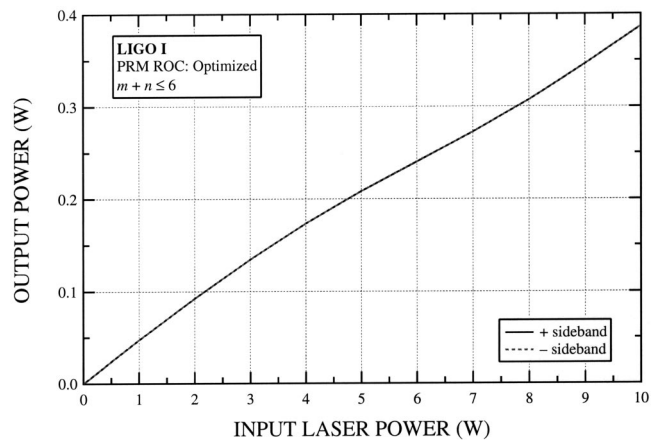


Fig. 17. Optimized initial LIGO antisymmetric ("dark") port output sideband powers as a function of total TEM_{00} input laser power. At each value of the input power, the PRM radius of curvature shown in Fig. 15 has been used.

15. Again, we have assumed a modulation depth of 0.47, which pushes $\sim 10\%$ of the total available laser power into the sidebands. The corresponding optimized initial LIGO recycled and output sideband powers are shown in Fig. 16 and Fig. 17, respectively. Note that at each value of the input power in these two plots, the corresponding PRM ROC shown in Fig. 15 has been used. Although the residual imbalance of the recycled sideband fields remains at the 3–4% level at an input power of 10 W, the imbalance at the antisymmetric port is negligible.

As an example of the operating characteristics of a fixed interferometer design point, Fig. 18 and Fig. 19 give the recycled and output powers at the carrier and sideband modulation frequencies for an interferometer optimized for a total laser input power of 6.5 W. The optimum PRM ROC is 12.281 km, and, as shown in Fig. 18, the recycling gain for the carrier is ~ 50 . Figure 19 predicts that, at 6.5 W, the sidebands are approximately balanced, with ~ 255 mW in each field, while the total carrier power emerging from the dark port is ~ 10 μ W. Approximately 90% of this carrier power is stored in higher-order

modes. Note that this optimum PRM ROC value is ~ 2.6 km shorter than the value of 14.9 km specified in the initial LIGO I reference design, primarily because of the sensitivity of this parameter to the method chosen for sideband rebalancing, the recycling gain, the thermo-optic coefficient $d\eta/dT$ of the substrate, and the substrate and coating absorption coefficients.

The behavior of the idealized PRFPMI phase-control system is illustrated in Fig. 20. The PRM (\mathcal{M}_5) is initially pulled in toward the beam splitter to compensate for the longitudinal phase introduced by the mismatch between the curvatures of the field emerging from the parallel FPI and the PRM itself. However, as the strengths of the thermal lenses in the ITM substrates increase, the mirror is pushed away from the beam splitter to maintain the carrier resonance. Similarly, as the astigmatic thermal lens develops in the beam-splitter substrate, the beam splitter moves slightly toward the lower right in Fig. 1. Indeed, as we see in Fig. 21, even in the y - z plane, the effective focal length of the beam-splitter substrate is six times larger than that of either ITM substrate; nevertheless, the resulting asymmetry between the two Michelson arms is numerically detected and compensated.

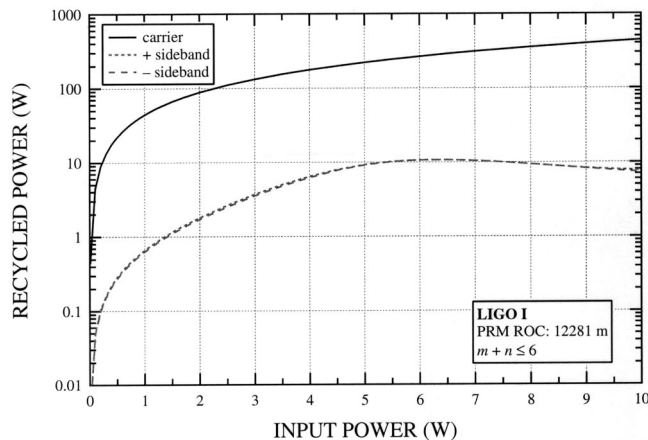


Fig. 18. Initial LIGO recycled powers as a function of total TEM_{00} input laser power.

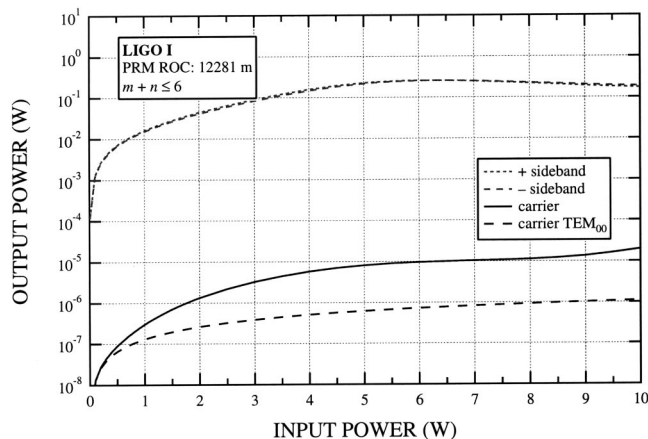


Fig. 19. Initial LIGO antisymmetric (“dark”) port output powers as a function of total TEM_{00} input laser power.

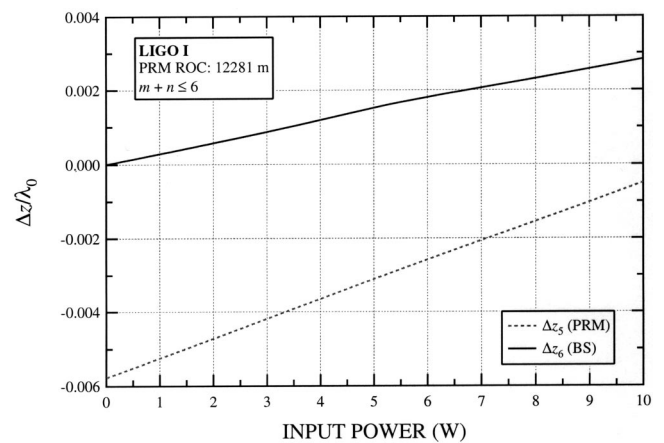


Fig. 20. Initial LIGO PRM and beam-splitter microdisplacements as a function of total TEM_{00} input laser power.

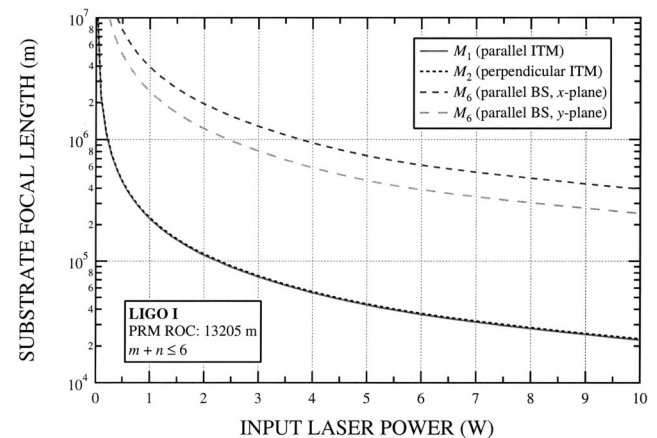


Fig. 21. Initial LIGO effective (i.e., quadratic) thermal focal lengths as a function of total TEM_{00} input laser power.

4. CONCLUSION

We have developed highly detailed steady-state analytical and numerical models of the physical phenomena that limit the intracavity power enhancement of recycled Michelson Fabry–Perot laser gravitational-wave detectors. We have included in our operator-based formalism the effects of nonlinear thermal lensing due to power absorption in both the substrates and coatings of the mirrors and beam splitter, the effects of any mismatch between the curvatures of the laser wave front and the mirror surface, and the diffraction by an aperture at each instance of reflection and transmission. We have taken great care to preserve numerically the nearly ideal longitudinal phase resonance conditions that would otherwise be provided by an external servo-locking control system. Once the mirrors and beam splitters have been analyzed and their transfer matrices constructed, more complicated optical components and structures (such as Fabry–Perot and Michelson interferometers, and the LIGO detector) can be modeled by simple matrix composition.

Our formalism relies on the validity of an expansion of the intracavity electromagnetic field at any reference plane in a necessarily incomplete set of possibly biorthogonal basis functions that are derived from eigenmodes of one of the Fabry–Perot arm cavities. In two

specific cases, we have checked the results produced by Melody, a fast MATLAB implementation of our model, against those generated by an FFT program used to model optical imperfections in LIGO. We have found that Melody can accurately predict the behavior of the carrier even in highly perturbed cold resonators with a modest number of spatial basis functions in orders of magnitude less time than is required by the FFT code. The same is true for the sideband fields stored in the power-recycling cavity, except in the case where the recycling cavity is significantly geometrically unstable. Even in this situation, which does not arise when the interferometer is thermally loaded, accuracy can be improved substantially by including more modes in the simulation.

We have discovered and described in broad terms the conditions under which the power stored in the two sideband fields can become unbalanced, potentially affecting the noise sensitivity of the gravitational-wave interferometer in the detection band. At this point, we have identified two possible (but potentially difficult to implement) solutions to this problem that will allow a reduction of the sideband imbalance at the expense of a previously optimized optical property of the carrier field. In our numerical simulations, we have found that, under conditions similar to the operating characteristics of initial LIGO, the optimum PRM ROC is only 12.3 km (for balanced sidebands), rather than the value of 14.9 km specified in the initial LIGO I reference design. Clearly, the precise value of the optimum PRM ROC depends sensitively on the method chosen for sideband rebalancing, the recycling gain, the thermo-optic coefficient $d\eta/dT$ of the substrate, and the substrate and coating absorption coefficients.

In the future, we will include the effects of thermoelastic surface deformation in our model and apply it to proposed configurations of the advanced LIGO interferometer. Other systematic perturbations and imperfections (e.g., mirror tilt and transverse displacement) can be included easily by incorporating the appropriate operators into the transfer matrices describing reflection and transmission for the mirrors and beam splitter. In addition, we intend to develop algorithms for the simulation of the optical response of an interferometer to gravitational radiation, with the intention of estimating the detection sensitivity of advanced LIGO under full thermal load. We anticipate that the performance of the Melody program will not be significantly affected by these modifications.

ACKNOWLEDGMENTS

We thank Ryan Lawrence for providing us with the finite-element software used to compute the temperature distributions in the LIGO beam splitter and for updated measurements of the emissivity and $d\eta/dT$ of fused silica. We are grateful to the Center for Advanced Computing Research for providing the supercomputer facilities and the CPU time to execute our FFT codes. This work has been partially supported by the National Science Foundation under Cooperative Agreement PHY-9210038.

*Visiting scientist. Permanent address: HP Laboratories, 13837 175th Pl. NE, Redmond, Washington 98052-2180. Electronic address: beausol@hpl.hp.com.

REFERENCES

1. C. M. Will, *Theory and Experiment in Gravitational Physics*, revised ed. (Cambridge University, Cambridge, England, 1993).
2. D. G. Blair, ed., *The Detection of Gravitational Waves* (Cambridge University, Cambridge, England, 1993).
3. P. R. Saulson, *Fundamentals of Interferometric Gravitational Wave Detectors* (World Scientific, Singapore, 1994).
4. A. Abramovici, W. Althouse, R. Drever, Y. Gursel, S. Kawamura, F. Raab, D. Shoemaker, L. Sievers, R. Spero, K. Thorne, R. Vogt, R. Weiss, S. Whitcomb, and M. Zucker, "LIGO: The laser interferometer gravitational-wave observatory," *Science* **256**, 325–333 (1992).
5. A. Abramovici, W. Althouse, J. Camp, J. A. Giaime, A. Gillespie, S. Kawamura, A. Kuhnert, T. Lyons, F. J. Raab, R. L. Savage Jr., D. Shoemaker, L. Sievers, R. Spero, R. Vogt, R. Weiss, S. Whitcomb, and M. Zucker, "Improved sensitivity in a gravitational wave interferometer and implications for LIGO," *Phys. Lett. A* **218**, 157–163 (1996).
6. A. Giazotto, "The VIRGO experiment: status of the art," in *First Edoardo Amaldi Conference on Gravitational Wave Experiments*, E. Coccia, G. Pizella, and F. Ronga, eds. (World Scientific, Singapore, 1995), p. 86.
7. K. Danzmann, "GEO 600—a 600-m laser interferometric gravitational wave antenna," in *First Edoardo Amaldi Conference on Gravitational Wave Experiments*, E. Coccia, G. Pizella, and F. Ronga, eds. (World Scientific, Singapore, 1995), p. 100.
8. K. Tsubono, "300-m laser interferometric gravitational wave detector (TAMA300) in Japan," in *First Edoardo Amaldi Conference on Gravitational Wave Experiments*, E. Coccia, G. Pizella, and F. Ronga, eds. (World Scientific, Singapore, 1995), p. 112.
9. R. W. P. Drever, J. L. Hall, F. V. Kowalski, J. Hough, G. M. Ford, A. J. Munley, and H. Ward, "Laser phase and frequency stabilization using an optical resonator," *Appl. Phys. B* **31**, 97–105 (1983).
10. P. Fritschel, R. Bork, G. Lez, N. Mavalvala, D. Ouimette, H. Rong, D. Sigg, and M. Zucker, "Readout and control of a power-recycled interferometric gravitational-wave antenna," *Appl. Opt.* **40**, 4988–4998 (2001).
11. B. J. Meers and K. A. Strain, "Wave-front distortion in laser-interferometric gravitational-wave detectors," *Phys. Rev. D* **43**, 3117–3130 (1991).
12. W. Winkler, K. Danzmann, A. Rüdiger, and R. Schilling, "Heating by optical absorption and the performance of interferometric gravitational-wave detectors," *Phys. Rev. A* **44**, 7022–7036 (1991).
13. K. A. Strain, K. Danzmann, J. Mizuno, P. G. Nelson, A. Rüdiger, R. Schilling, and W. Winkler, "Thermal lensing in recycling interferometric gravitational wave detectors," *Phys. Lett. A* **194**, 124–132 (1994).
14. D. McClelland, J. Camp, J. Mason, W. Kells, and S. Whitcomb, "Arm cavity resonant sideband control for laser interferometric gravitational wave detectors," *Opt. Lett.* **24**, 1014–1016 (1999).
15. J.-Y. Vinet, P. Hello, C. N. Man, and A. Brillet, "A high-accuracy method for the simulation of non-ideal optical cavities," *J. Phys. I* **2**, 1287–1303 (1992).
16. P. Saha, "Fast estimation of transverse fields in high-finesse optical cavities," *J. Opt. Soc. Am. A* **14**, 2195–2202 (1997).
17. B. Bochner, "Modeling the performance of interferometric gravitational-wave detectors with realistically imperfect optics," Ph.D. dissertation (Massachusetts Institute of Technology, Cambridge, Mass., 1998).
18. P. Hello and J.-Y. Vinet, "Analytical models of thermal ab-

- errations in massive mirrors heated by high power laser beams," *J. Phys. (Paris)* **51**, 1267–1282 (1990).
19. D. Z. Anderson, "Alignment of resonant optical cavities," *Appl. Opt.* **23**, 2944–2949 (1984).
 20. E. Morrison, B. J. Meers, D. I. Robertson, and H. Ward, "Automatic alignment of optical interferometers," *Appl. Opt.* **33**, 5041–5049 (1994).
 21. Y. Hefetz, N. Mavalvala, and D. Sigg, "Principles of calculating alignment signals in complex resonant optical interferometers," *J. Opt. Soc. Am. B* **107**, 1597–1605 (1997).
 22. R. G. Beausoleil and D. Sigg, "Spatiotemporal model of the LIGO interferometer," *J. Opt. Soc. Am. A* **16**, 2990–3002 (1999).
 23. A. E. Siegman, *Lasers* (University Science, Mill Valley, Calif., 1986); errata URL: http://www-ee.stanford.edu/~siegman/lasers_book_errata.txt.
 24. K. E. Oughstun, in *Progress in Optics*, E. Wolf, ed. (North-Holland, Amsterdam, 1987), Vol. 24, pp. 165–387.
 25. A. Kostenbauder, Y. Sun, and A. E. Siegman, "Eigenmode expansions using biorthogonal functions: complex-valued Hermite–Gaussians," *J. Opt. Soc. Am. A* **14**, 1780–1790 (1997).
 26. See <http://www.mathworks.com/products/matlab/>.
 27. The Melody/MATLAB software package can be downloaded from the LIGO Software Tools for Advanced Interferometer Configurations Internet web site at the URL <http://www.phys.ufl.edu/LIGO/LIGO/STAIC.html>.
 28. See <http://www.ligo.caltech.edu/gari/COCAsBuilt.htm>.